Calorimetric and Dielectric Investigations of Epoxy-Based Nanocomposites with Halloysite Nanotubes as Nanofillers

Hassan Omar [1], Glen J. Smales [1], Sven Henning [2], Zhi Li [3,†], De-Yi Wang [3], Andreas Schönhals [1] and Paulina Szymoniak [1,*]

[1] Bundesanstalt für Materialforschung und -prüfung (BAM), Unter den Eichen 87, 12205 Berlin, Germany; hassan.omar@bam.de (H.O.); glen-jacob.smales@bam.de (G.J.S.); andreas.schoenhals@bam.de (A.S.)
[2] Fraunhofer-Institut für Mikrostruktur von Werkstoffen und Systemen (IMWS), Walter-Hülse-Str. 1, 06120 Halle, Germany; sven.henning@imws.fraunhofer.de
[3] IMDEA Materials Institute, C/Eric Kandel 2, 28906 Getafe, Spain; zhi.li@cqjtu.edu.cn (Z.L.); deyi.wang@imdea.org (D.-Y.W.)
* Correspondence: paulina.szymoniak@bam.de
† Current address: China-Spain Collaborative Research Center for Advanced Materials, School of Materials Science and Engineering, Chongqing Jiaotong University, Chongqing 400074, China.

Abstract: Epoxy nanocomposites are promising materials for industrial applications (i.e., aerospace, marine and automotive industry) due to their extraordinary mechanical and thermal properties. Here, the effect of hollow halloysite nanotubes (HNT) on an epoxy matrix (Ep) was the focus of the study. The structure and molecular mobility of the nanocomposites were investigated using a combination of X-ray scattering, calorimetry (differential (DSC) and fast scanning calorimetry (FSC)) and dielectric spectroscopy. Additionally, the effect of surface modification of HNT (polydopamine (PDA) and $Fe(OH)_3$ nanodots) was considered. For Ep/HNT, the glass transition temperature (T_g) was decreased due to a nanoparticle-related decrease of the crosslinking density. For the modified system, Ep/m-HNT, the surface modification resulted in enhanced filler–matrix interactions leading to higher T_g values than the pure epoxy in some cases. For Ep/m-HNT, the amount of interface formed between the nanoparticles and the matrix ranged from 5% to 15%. Through BDS measurements, localized fluctuations were detected as a β- and γ-relaxation, related to rotational fluctuations of phenyl rings and local reorientations of unreacted components. A combination of calorimetry and dielectric spectroscopy revealed a dynamic and structural heterogeneity of the matrix, as confirmed by two glassy dynamics in both systems, related to regions with different crosslinking densities.

Keywords: epoxy nanocomposites; halloysite nanotubes; X-ray scattering; differential scanning calorimetry; broadband dielectric spectroscopy; flash DSC; rigid amorphous fraction

1. Introduction

Polymer nanocomposites (PNCs) are systems composed of two or more components where the matrix is a polymer and the incorporated nanofillers have at least one dimension on the nanometer scale (<100 nm) [1]. PNCs have attracted considerable attention due to their improved properties (e.g., mechanical strength, toughness, electric and thermal conductivity and flame retardancy) compared to the unfilled polymer [2]. These improved properties can be achieved with low filler content, so that the system retains its low weight and ease of processability [2,3]. Additionally, by varying the type of filler and polymer matrix, and thereby the polymer–filler interactions, the properties of the PNC system can be tuned for specific purposes, thus providing the possibility of tunable nanocomposite systems [4].

The performance of a PNC, in parallel with the characteristics of the used components, depends on the size, the aspect ratio, the surface area and the weight fraction of

the nanofiller. However, the most important factors are the dispersion of the nanofiller (filler–filler interactions) and the interfacial region formed between the bulk matrix and the nanofiller (filler–polymer interactions) [5]. The dispersion of nanofillers can be homogenous in the matrix but might also be associated with the formation of agglomerates. This results from short-range interactions such as van der Waals forces between the primary particles [6]. Aggregation can be controlled to a certain extent by employing specific sample preparation steps. The use of severe shear stress and surface modification of the filler have been shown to result in a homogenous particle dispersion in the polymer matrix [7]. On the one hand, a good dispersion of nanofillers has resulted in improved diffusion of solvents, heat deflection temperature and other thermal properties [8]. Moreover, aggregation can introduce defects and stress concentrations that have adverse effects on the mechanical properties [9]. On the other hand, aggregation has been shown to be related to a reinforcement of PNC properties in some cases [10].

Furthermore, "interfacial properties" have been found to have a significant contribution to the properties of PNCs. Due to the reduced dimensions of the filler, resulting in a high surface to volume ratio, there is an increased volume of interfacial area. For non-repulsive filler–matrix interactions, polymer segments are physically adsorbed to the nanofiller, with the formed interphase commonly referred to as the rigid amorphous fraction (RAF) [11]. The RAF can also be formed through chemical bonding of the nanoparticle surface to the matrix. The properties of the RAF may differ from those of the bulk matrix such as conformations, density and molecular mobility. The term "rigid" refers to a restricted or even immobilized segmental mobility in the interface compared to the bulk matrix [12]. The different molecular mobility at the interface, compared to the bulk matrix, can be investigated using broadband dielectric spectroscopy (BDS) in some cases [11–14]. Moreover, BDS allows for the investigation of the dynamical processes of PNCs in dependence on the concentration of the nanofiller on spatial length scales ranging from local to segmental fluctuations in a broad frequency range (mHz to GHz) [15]. Furthermore, one of the most useful techniques used to investigate filler-related effects on the polymer matrix is calorimetry. The glass transition temperature (T_g) can be investigated using differential scanning calorimetry [16] and fast scanning calorimetry [17]. Moreover, by analyzing the change in the specific heat capacity at the glass transition (calorimetric strength) using modulated DSC (TMDSC) [18], the amount of RAF and/or the number of mobilized segments due to the nanofiller in the system can be quantified [19].

In this study, two epoxy nanocomposite systems based on bisphenol-A-diglycidyl ether (DGEBA) were investigated. Epoxies were formed during a curing reaction, resulting in a crosslinked structure, which could be altered depending on the reactants and curing time. These systems have various applications in adhesives, coatings, electronics and as construction materials in automotive as well as aerospace industries [5,20,21]. They have good mechanical strength, Young's modulus and can be tailored for specific applications by tuning the crosslinking density. However, due to their brittleness and relatively high flammability, epoxy-based materials are commonly reinforced with inorganic particles to improve such properties [22,23].

Epoxy-based materials have been reinforced with nanoparticles (NPs), such as silica, barium titanate [24,25] or boehmite NPs [26,27], layered materials [11,28], polyhedral oligomeric silsesquioxane (POSS) [29,30] and carbon nanotubes (CNT) [31,32], to achieve improved properties compared to the unfilled epoxy. CNTs have been used as a nanofiller due to their high aspect ratio, having a significantly larger length compared to the inner and outer diameters, ease of processing and their ability to be surface modified [33]. In addition, the incorporation of CNTs leads to enhancements in several properties of PNCs, such as increased mechanical, electrical and thermal characteristics. Recently, halloysite nanotubes (HNT) have gained attention as a cheaper, less toxic and more environmentally friendly alternative to CNTs, while possessing a similar crystal structure and aspect ratio [7,34]. The literature shows that the incorporation of HNTs into a polymer matrix can result in improvements in thermal and mechanical stability, biocompatibility, flame retardancy and

waterproof behavior, among other properties [35–39]. Li et al. showed an increase in both the storage modulus and tensile strength for an epoxy nanocomposite containing HNT, compared to an unfilled epoxy [36]. In addition, Ye et al. demonstrated that, with 2.3 wt.% HNT, the impact strength of the PNC is increased four-fold [37]. Lastly, HNTs can be incorporated without requiring intercalation or exfoliation into an epoxy matrix [7]. As a result of the growing interest and promising properties, pristine HNT was used as a nanofiller for this investigation. However, HNT has been shown in epoxies to form isolated clusters or agglomerates that can reach sizes up to several microns and cause deterioration in some mechanical properties [40]. This results from their external surface being largely composed of SiO_2 groups. Therefore, as the epoxy and the hydroxyl groups of DGEBA are inert towards aluminols and siloxanes under the curing conditions, the interfacial interaction between HNTs and the matrix can be considered as weak [41]. Various techniques have been used to break up these clusters including ball mill homogenization, ultrasonification and surface modification [7,42]. For the latter, it has been demonstrated that surface modification of the nanofillers improves its interactions with the polymer matrix and hence the properties of the nanocomposites [43,44]. For instance, surface modification using poly-dopamine (PDA), completed through a simple single-step technique, can be applied onto a wide range of inorganic and organic materials [45]. Dopamine is a neurotransmitter found in the human body and can self-polymerize on the surface of a material to form PDA. This leads to a formation of a nanoscale thin film that can be additionally modified for specific applications [46]. Here, dopamine was used to form a thin layer on the surface of HNT. It provided large quantities of hydroxyl groups to support the interfacial bonding and force a better dispersion of the nanofiller in the epoxy matrix [44]. Ultrafine iron trihydroxide ($Fe(OH)_3$) nanoparticles (size < 4 nm) were used to endow the PDA-coated HNT nanofillers with improved fire retardancy compared to unmodified HNT. $Fe(OH)_3$ nanoparticles have enhanced catalytic abilities due to the exposure of the iron atoms, resulting in a significant increase in both char yield and maximum degradation rate [44]. Although $Fe(OH)_3$ is linked to HNT, the nanocomposite with the modified HNT can be considered as a system that contains two different nanoparticles.

The methodology used to study both epoxy-based nanocomposite systems include a combination of conventional differential scanning calorimetry, fast scanning calorimetry, specific heat spectroscopy (SHS) in the form of temperature modulated DSC and FSC (TMFSC) and broadband dielectric spectroscopy. These techniques are used to obtain information about the structure, vitrification kinetics and molecular mobility of the un-modified and surface modified system. In addition, the dispersion and dimensions of the nanofiller were acquired from X-ray scattering and supplemented by transmission electron microscopy (TEM). The data obtained for both systems were directly compared to each other to reveal the effect of the modification on the dispersion and interphase formation. Up to this time, no studies are available on an epoxy-based PNC reinforced with HNT or modified HNT (m-HNT) as a filler using these techniques. To the best of our knowledge, until now, the molecular mobility and interfacial properties have not been discussed for the considered materials.

2. Materials and Methods

2.1. Materials

The investigated systems are based on bisphenol-A-diglycidyl ether (DGEBA, Epoxy-dharz C, Faserverbundwerkstoffe Composite Technology, Waldenbuch, Germany) cured with diethylenetriamine (DETA, Sigma-Aldrich, St. Louis, MO, USA). Halloysite nanotubes (HNT, Benahadux Company, Almeria, Spain) were used as the nanofiller. Iron trichloride ($FeCl_3$), dopamine hydrochloride (DA-HCl) and urea were obtained from Sigma-Aldrich. The sample preparation is shortly summarized here but described in detail by Li et al. [36]. For chemical details, the reader is referred to the work in [36].

HNT is an aluminosilicate with the chemical formula $Al_2Si_2O_5(OH)_4 \cdot nH_2O$, where, when $n = 2$, HNT is normally in a hydrated state with a layer of water molecules in the

interlayer space [44]. HNT has a hollow tubular structure with the outer surface chemically similar to the SiO_2 [41,47]. The design and chemical structure of HNT is given in Figure 1, where the exterior surface contains siloxane groups and the interior surface has aluminol groups. The length of the tubes ranges from 200 nm to 2 μm, as reported in [44] and addressed below.
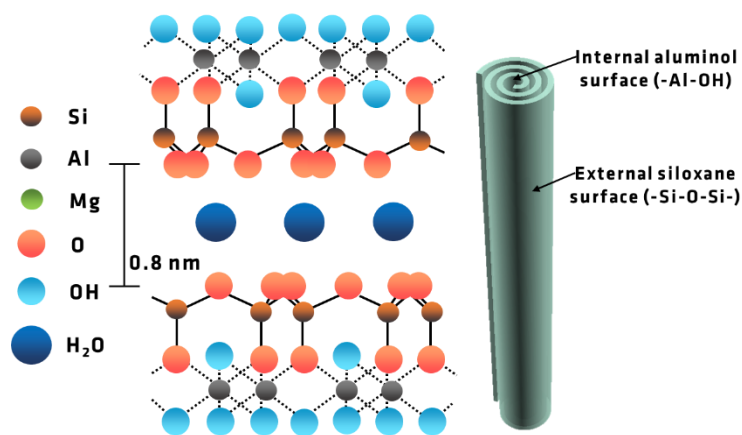

Figure 1. HNT structure with the layers and chemical structure detailed for HNT. Adapted from ref [48].

The interfacial bonding of the exterior hydroxyl groups of unmodified HNT was found to be insufficient to create a good connection to the epoxy and, hence, needed to be improved. Therefore, dopamine (DA) was used to form a nanocoating layer of poly-dopamine which has also been shown to increase dispersion of the filler in the matrix [41]. Moreover, the hydroxyl groups of PDA allow for better interactions with the matrix by forming strong hydrogen bonds with the epoxide groups of DGEBA. The modified HNT nanofillers were prepared by first coating them with DA by adding it into a buffer solution (tris(hydroxymethyl)aminomethane, concentrated hydrochloric acid and deionized water) containing the HNT for 24 h at ambient temperature. The obtained product (HNT@PDA) was decorated with ultrafine $Fe(OH)_3$ nanodots (size < 4 nm) via a urea-assisted approach. The final system was called HNT@PDA@$Fe(OH)_3$ or m-HNT.

Prior to the preparation of the composites, the HNT was dried at 353 K to remove adsorbed water. Unmodified and modified PNCs with varying concentrations were prepared by mixing the epoxy resin with selected amounts of the nanofiller. Next, DETA was added under vigorous stirring. The systems were then cast into a mold and cured for 24 h at 298 K. Lastly, the temperature was increased to 393 K and deep cured for 2 h. The resulting samples were named as Ep/HNTX and Ep/m-HNTX, where X represents the nominal weight concentration of HNT or m-HNT. For the pure Ep sample, the same curing condition was used as stated above.

2.2. Methods

2.2.1. Transmission Electron Microscopy (TEM)

TEM measurements were performed using an FEI TECNAI G2 transmission electron microscope (FEI Corporation, Hillsboro, OR, USA) in bright field mode with an acceleration voltage of 200 kV. Samples were prepared by cutting ultrathin slices (70 nm) using a cryo Leica Ultracut UCT ultramicrotome (Leica Microsystems GmbH, Wetzlar, Germany) with a Diatome diamond knife (Diatome Ltd., Bienne, Switzerland).

2.2.2. Small- and Wide-Angle X-ray Scattering (SAXS and WAXS)

The SAXS/WAXS measurements were carried out using MOUSE (Methodology Optimization for Ultrafine Structure Exploration). The X-rays were generated from monochromatized X-ray tubes with Cu Kα (λ = 0.154 nm) and Mo Kα (λ = 0.071 nm) (Xenocs, Grenoble, France). By utilizing two different X-ray sources, it was possible to avoid difficulties with

fluorescence from the iron of the m-HNT samples. Data collection was performed using an in-vacuum Eiger 1 M detector (Dectris, Baden-Daettwil, Switzerland), which was placed at multiple distances between 138 and 2507 mm from the sample. The resulting data were processed and scaled to absolute intensity values using the DAWN software package according to standardized procedures considering the propagation of errors [49,50]. Pure epoxy, HNT, m-HNT and PNC systems (Ep6/HNT, Ep12/HNT, Ep15/HNT, Ep6/m-HNT and Ep15/m-HNT) were investigated employing this technique.

2.2.3. WAXS: Linear Combination of the Data for the Pure Epoxy and the Nanofiller

As the SAXS/WAXS data were scaled to absolute intensity, it was possible to perform a linear combination of Ep and HNT/m-HNT WAXS data to obtain a rough estimate of the volume fractions for both components [11,27]. For the HNT and m-HNT samples, data were collected using two different X-ray sources (Xenocs, Grenoble, France), in multiple sample positions, with no observed change in the ratio of peak intensities, indicating that the measured samples lack orientation, and a decent powder diffraction average signal was collected. This also remained true for the PNC samples with HNT and m-HNT particles embedded within the epoxy. Hence, a linear combination was performed along a q-range of 6–50 nm^{-1}. From the obtained scaling factors (from a least-squares optimization), a rough volume fraction was determined for both the epoxy and the HNT/m-HNT present in PNCs. For this analysis, epoxy, HNT and m-HNT were assumed to have atomic compositions of $C_{47}H_{56}O_9N$ (1.13 g cm^{-3}), $Al_2H_2O_9Si$ (2.4 g cm^{-3}) and $Al_2H_5O_{12}SiFe$ (2.708 g cm^{-3}), respectively.

2.2.4. SAXS Pattern Simulations from 3D Objects

SPONGE, a scattering pattern calculator written in Python (Python Software Foundation, Wilmington, DE, USA), was utilized to verify features observed in the SAXS patterns from simulations of rolled cylinders [51–53]. SPONGE can calculate scattering patterns from three-dimensional objects, with the ability to add polydispersity and structural dynamics to the system, while staying as close as possible to the first principles of scattering. It utilized the Debye equation to calculate the scattering patterns from randomly distributed, infinitesimally small points, randomly distributed inside of the object surface [54,55].

For this analysis, three-dimensional rolled cylinders were generated in OpenSCAD and exported to STL files (STereo Lithography) [56]. Different models were generated to show how the different structural parameters affect the simulated SAXS patterns. Changes to the length (D_{length}), outer diameter (D_{outer}), Lumen diameter (number of rolls) (D_{lumen}) and thickness of the rolled sheet (D_{sheet}) were probed, as well as polydispersity (σ) (Gaussian size distribution). All parameters were kept constant between simulations except the specific parameter being changed. As a base model, the following parameters were used: length = 100 nm, outer diameter = 13 nm, lumen diameter = 5 nm and thickness = 1 nm. This base model was also used to investigate polydispersity with a Gaussian distribution, with values of the standard deviation (σ) between 0.1 and 0.5. In general, the SPONGE simulations were performed with 1000 points inside the rolled cylinders, 200 points logarithmically divided along the q-vector within 0.018–20 nm^{-1} and 500 independent repetitions of the simulation.

2.2.5. Differential Scanning Calorimetry (DSC)

The conventional DSC measurements were performed by a power compensated Perkin Elmer DSC 8500 instrument (Perkin Elmer, Waltham, MA, USA) with a heating/cooling rate of 10 K min^{-1} in the temperature range of 298–493 K. Samples with masses of ca. 8.5 $\pm$ 0.2 mg were placed in 50 μL aluminum pans. The data of the second heating run were taken for analysis to allow the samples to be completely cured for a detailed comparison of the results. Nitrogen was used as the protection gas at a flow rate of 20 mL min^{-1}. Baseline corrections were performed by measuring empty pans where this data was subtracted from that of the samples. Temperature and heat flow calibration was performed using indium

as a standard. Each sample was measured approximately 3 times and the error in T_g was below 2 K.

2.2.6. Temperature Modulated DSC (TMDSC)

TMDSC was carried out using a Perkin Elmer DSC 8500 device (Perkin Elmer, Waltham, MA, USA), employing the StepScan® approach, where alternating steps of heating and isothermal times were applied, resulting in a periodic heat flow. A heating rate of 60 K min^{-1} with a step height of 2 K was used. The length of the isothermal steps resulted in frequencies between 8.3×10^{-3} and 3.3×10^{-2} Hz (isotherm times from 120 to 30 s). Nitrogen was used as a purge gas at a flow rate of 20 mL min^{-1}. The complex specific heat capacity (c_p*) was estimated as the area under the heat flow peak divided by the height of the predefined temperature step. Absolute values of the heat capacity were obtained by synthetic sapphire as reference material. The modulus of complex specific heat capacity $\left| c_p^* \right| = \sqrt{c_p'^2 + c_p''^2}$ (the so-called reversing heat capacity) was considered, where c_p' and c_p'' are the real and imaginary parts of c_p^*.

2.2.7. Fast Scanning Calorimetry (FSC)

FSC was used to extend the vitrification investigations to higher heating rates. A Mettler Toledo Flash DSC 1 (Mettler Toledo, Greifensee, Switzerland), a chip-based power compensated DSC, was used in conjunction with micro electrical mechanical systems (MEMS) sensors to allow heating rates up to 4×10^4 K^{-1}. For each sample, a specific non-adiabatic chip sensor was used with an active reference and the sample site. The samples were prepared by cutting 10 μm thick pieces using a cryo-microtome. Since thermosetting materials are unable to be melted, the high viscosity silicon oil AK 60,000 from Wacker Chemie AG (Burghausen, Germany) was used to improve the thermal contact between the sample and sensor and to reduce the thermal lag. Silicon oil was placed on both the sample and reference sensors to account for its additional heat capacity in the measurements. For the investigations of the glass transition, the data from cooling is commonly used. However, the thermal lag was insignificant between heating and cooling due to the small sample dimensions. Therefore, here the data of the heating run were used. Nitrogen was used as a purge gas at a flow rate of 40 mL min^{-1}.

2.2.8. Temperature Modulated FSC (TMFSC)

This technique is based on the Mettler Toledo Flash DSC 1. Similar to TMDSC, a modulated temperature profile was applied by heating and isothermal steps. The complex heat capacity (C_p^*) was obtained as Fourier transformation of the instantaneous heat flow (HF) over the Fourier transform of the heating rate ($\dot{T}$).

$$C_p^* = \frac{\int_0^{t_p} HF(t)e^{-i\omega t}dt}{\int_0^{t_p} \dot{T}(t)e^{-i\omega t}dt} \tag{1}$$

where w is the angular frequency. For these investigations a step height of 2 K with heating rates of 200 and 2000 K/s were used with isothermal times t_p = 1, 0.1 and 0.05 s. The frequency ($f = \frac{2\pi}{\omega}$) was noted as the inverse of each isothermal time. The sparse fast Fourier transformation (SFFT) was employed, which gives also higher harmonic frequencies (from 1 to 11 Hz for 1 s, from 10 to 110 Hz for 0.1 s and from 20 to 220 Hz for 0.05 s). Again, the modulus of the complex heat capacity was used for analysis.

2.2.9. Broadband Dielectric Spectroscopy (BDS)

BDS was used to investigate the molecular mobility of the materials in the frequency range from 10^{-1} to 10^6 Hz [15,57]. A periodic electric field with a small field strength was applied as an input and the time-dependent polarization was measured as output. The polarization arises from the orientation of permanent dipoles in the material and can

be quantified using the complex dielectric function $\varepsilon^*(\omega) = \varepsilon'(\omega) - i\varepsilon''(\omega)$ where $\varepsilon'(\omega)$ is the real (storage) part of the complex dielectric function and $\varepsilon''(\omega)$ is the imaginary (loss) part. The dielectric properties of the samples were measured in the temperature range from 173 to 503 K. BDS was carried out by a Novocontrol high-resolution ALPHA analyzer (Novocontrol Technologies, Montabaur, Germany) connected to an active sample cell. A Quatro Novocontrol cryosystem employing a temperature stability better than 0.1 K was used for temperature control. All samples were placed between two gold plated electrodes (Ø = 20 mm) in a parallel plate geometry. Gold electrodes were evaporated onto the surfaces of the samples in an ultrahigh vacuum (10^{-5} mbar) to establish a good electrical contact. The impedance $Z^*(\omega)$ was measured and the complex dielectric function was calculated from the impedance.

3. Results and Discussion

3.1. Epoxy Nanocomposite with Halloysite Nanotubes (Ep/HNT)

3.1.1. X-ray Scattering

To study the structure and morphology, X-ray scattering experiments were performed on pure epoxy, HNT and three nanocomposites (Ep/HNT6, Ep/HNT12 and Ep/HNT15). The scattering patterns are shown in Figure 2. The (001) peaks found for pure HNT (8.42 nm^{-1}) indicate layer spacings of 0.75 nm. However, these peaks are relatively broad indicating that there is distribution in the observed layer spacing, ranging between ca. 0.63 and 0.93 nm. The presence of the (020) reflection at 14.2 nm^{-1} indicates that the HNT sample is present in a dehydrated state and tubular in shape [58,59].
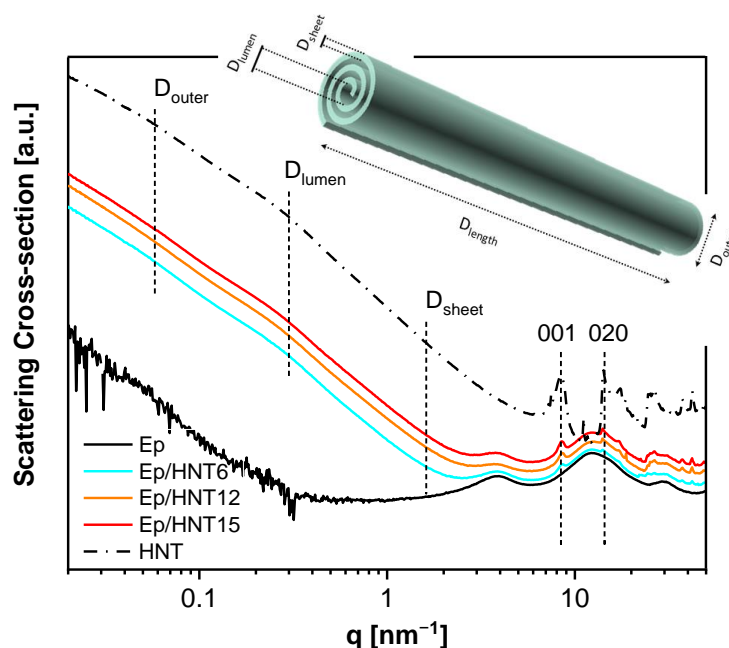

Figure 2. X-ray scattering patterns of the pure epoxy, halloysite nanotubes and nanocomposites as indicated. The curves are shifted along the *Y*-axis for the sake of clarity. The raw scattering data at absolute values of the scattering cross-section are shown in Figure S2. The inset gives a scheme of the halloysite rolled cylinder with different dimensions indicated.

The scattering pattern of the pure epoxy shows three distinct scattering features in the WAXS region, located at 3.88, 12.46 and 29.8 nm^{-1}. These broad bumps in the X-ray scattering patterns of amorphous materials with no long-range correlations can be taken as a fingerprint for short-range correlations within the epoxy [60]. A detailed analysis of the origin of the three-peak structure for an anhydride epoxy material can be found in [27], where such an X-ray scattering was related to an inherent spatial heterogeneity of the crosslinked network. The intermediate bump with the highest intensity, at q = 12.46 nm^{-1},

is the amorphous halo, corresponding to the most frequently occurring intermolecular distances. The peak at q = 3.88 nm^{-1} was assigned to isopropylidene groups between the phenyl rings forming elongated clusters with an average size of ca. 1.6 nm, in the Bragg approximation. The peak at q = 29.8 nm^{-1} (averaged intermolecular distances of ca. 0.21 nm) can be correlated with regions in the network with lower crosslinking density than the average, as discussed in [11].

For the composites, the position of the peaks related to the crystal structure of HNT remain unaffected, indicating that the nanotubes maintained approximately their structure upon incorporation in the matrix. Moreover, the amorphous halo and the two other broad features in the X-ray scattering are also found at the same positions as that for the pure epoxy. Therefore, it is concluded that X-ray investigations did not detect large differences in the structure of the matrix in the PNCs compared to the pure epoxy.

An example for the analysis of the WAXS data by the linear combination is shown in Figure 3. This analysis, carried out for Ep/HNT6, 12 and 15, revealed that the concentration of the HNT is lower than the nominal one (inset Figure 3). The calculated values from the WAXS data agree with the weight fractions obtained from thermogravimetric analysis (TGA, for details see the Supplementary Materials). This means both methods prove that the HNT concentration in the composites is lower than formulated.
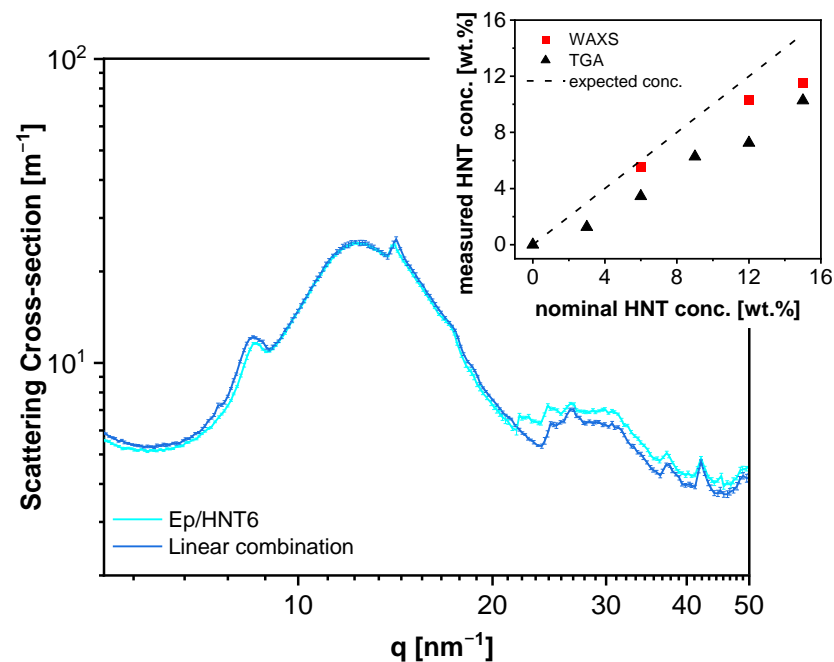

Figure 3. Analysis of the X-ray data for Ep/HNT6 in the WAXS region by fitting a linear combination of the pure epoxy and HNT nanotubes data. Experimental data, light blue; fit function, dark blue. The inset represents the weight fractions of the nanofiller estimated by X-ray scattering and thermogravimetric analysis as a function of the HNT nominal concentration. The dashed line represents the one-to-one relationship.

The SAXS data for HNT and the PNCs were analyzed using McSAS, a Monte Carlo fitting method for extracting form-free size distributions [50] (see Figure S3). From this analysis, three distinct size regimes were observed in the (volume-weighted) distributions, at ca. 4, 19 and 125 nm. To assign these values to the complex morphology of HNT, simulations of SAXS profiles from 3D models were performed. The simulated SAXS curves from 3D models with varying structural parameters can be seen in Figure S4. For these simulations, only a single parameter was altered each time to observe how each structural feature can affect the simulated SAXS profiles. Thus, it was possible to assign certain features of the SAXS data to different features in the rolled cylinders. Three

features are observed in the SAXS data, which are representative of D_{outer}, D_{lumen} and D_{sheet}, with D_{length} > 400 nm (inset Figure 3) being greater than that of the observable experimental SAXS range. It was found that the HNT within the PNCs has average dimensional properties of D_{outer} = ~125 nm, D_{lumen} = ~19 nm and D_{sheet} = ~4 nm. It was found that D_{outer} and D_{lumen} are different for the nanocomposites and the pure HNT. D_{outer} increases for the nanocomposites (~125 nm) by approximately 18 nm, compared to pure HNT (~ 107 nm), where D_{lumen} for the PNCs is ca. 19.2 nm, whereas for HNT it is ca. 19.7 nm. These changes in the outer and lumen diameter of the nanofiller embedded in the matrix, in comparison to the pure HNT, might be discussed in terms of a swelling of the NPs due to the entering of small molecules into the rolls. Considering that HNT is added to the reaction mixture before the crosslinking reaction it can be assumed that one or both components (DGEBA and/or DETA) enter the rolls of the tube, widening the overall diameter and decreasing the inside space of the tubular structure. Nevertheless, the distribution of D_{outer} values is quite broad, thus it cannot be excluded that larger D_{outer} is observed for PNCs than the pure filler due to a smoother electron density transition, leading to a greater power-law approximation in the simulations. These dimensions are complimentary to those seen by transmission electron microscopy (Figure 4) and those given in the literature [52,53]. To further confirm the observed features, simulations of larger rolled cylinders that more closely represent these parameters were undertaken. From these simulations, a good correlation between D_{outer} and D_{lumen} was observed. However, due to difficulties in the simulation of data at high q values and the implementation of a global polydispersity across the whole model (Gaussian distribution) in SPONGE, rather than the separation of polydispersity parameters across the different parameters as would be expected from real samples, correlating features towards higher-q becomes difficult to observe.
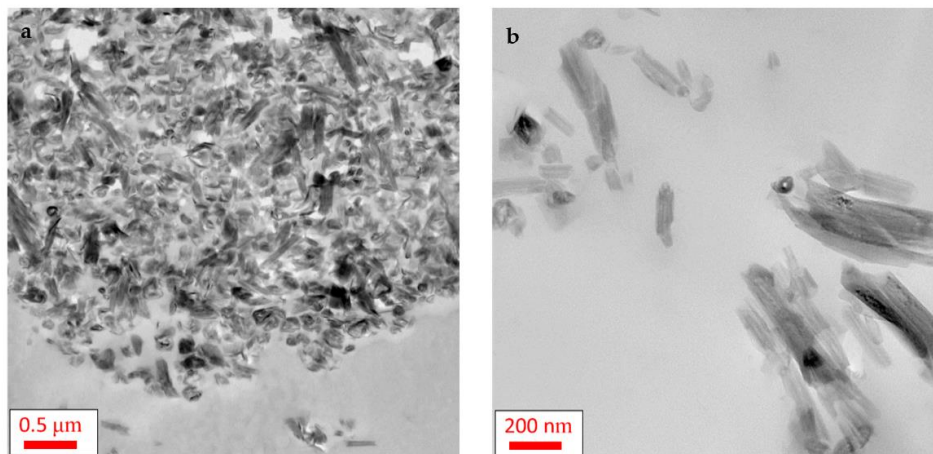

Figure 4. TEM images for Ep/HNT15: (**a**) lower magnification; and (**b**) higher magnification.

3.1.2. TEM

The morphology of the system was further investigated using transmission electron microscopy. Figure 4 shows the TEM images obtained for Ep/HNT15 at two different positions of the sample at two magnifications. Figure 4a, taken with a lower magnification, shows that HNTs are dispersed in agglomerates in the epoxy matrix, forming clusters on the length scale of some μm. For other regions, depicted in Figure 4b, the HNTs are dispersed more or less separately in the matrix. Moreover, the shape of the HNT is unaltered, maintaining the tubular shape when embedded in the matrix as also confirmed by the X-ray measurements. Additional TEM images were obtained for the pure epoxy and Ep/HNT6 (Figure S5).

3.1.3. Calorimetry

The thermal properties of the pure epoxy and the unmodified PNCs (Ep/HNT3–Ep/HNT15) were first investigated by conventional DSC. The normalized heat flow curves ($HF_{norm} = \frac{HF - HF_{glass}}{HF_{liquid} - HF_{glass}}$) are shown in Figure 5a. The second heating run was taken for analysis for the reasons discussed above. The glass transition temperature (T_g) was estimated by fitting a sigmoidal function to the heat flow curve measured at 10 K min^{-1}. Next, the derivative of the fit was taken with respect to temperature (Figure S6). A Gaussian was further fitted to the resulting peak and the maximum position of the Gaussian was taken as T_g. Figure 5b depicts the T_g values from DSC as a function of the nominal filler content for the heating rates of 10 K min^{-1}.
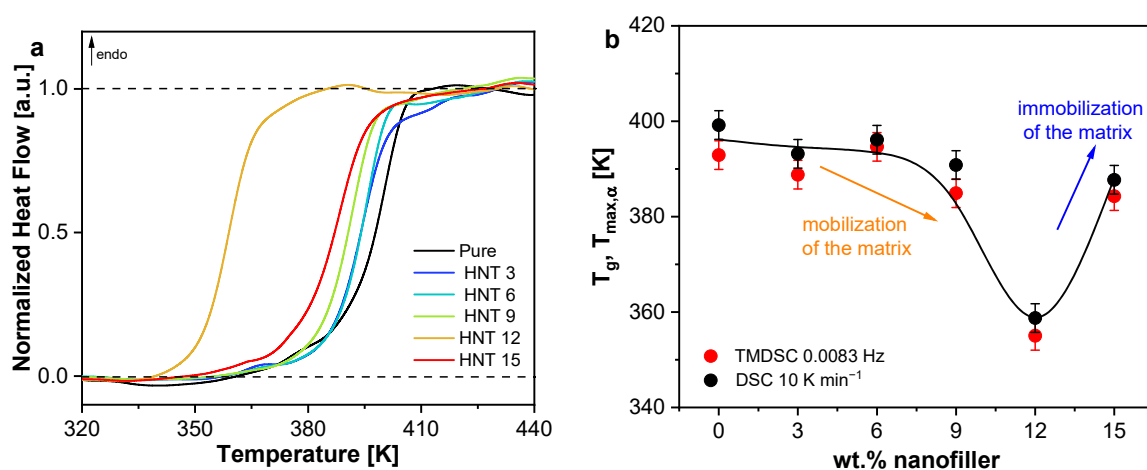

Figure 5. (**a**) Normalized heat flow curves as described in the text for the indicated materials. (**b**) Glass transition temperature as a function of the nominal filler content for conventional DSC and TMDSC, estimated as described in the text. Error bars are given and a line as a guide for the eyes for the DSC data.

The glass transition temperature decreases compared to the unfilled sample with increasing nominal nanofiller concentration till 12 wt.%, followed by an increase of T_g for 15 wt.% (see Figure 5b). The complex concentration dependence of T_g was observed for all employed thermal methods. It can be discussed to arise from two competing mechanisms: (1) a mobilization; and (2) an immobilization of segments of the epoxy matrix due to the nanofiller.

(1) The mobilization is related to a decrease in the crosslinking density of the epoxy due to the nanofillers, which are acting as spatial obstacles and affecting the diffusion-controlled curing reaction [27]. Hence, for all PNC concentrations, a reduction in crosslinking density should take place, and, thus, the glass transition temperature decreases compared to the unfilled epoxy. Another approach to discuss the reduced crosslinking density was a preferential adsorption and/or the intercalation of one reactant onto the nanofillers. Some amount of this reactant would then be unavailable for the curing reaction and also result in a lower crosslinking density. It should be noted that an intercalation of one of the reaction partners was suggested by the X-ray measurements. Furthermore, other scenarios of the mobilization of an epoxy-matrix by SiO$_2$-based nanofillers are discussed in the literature. Sun et al. investigated the effect of nanofillers on glass transition behavior for various epoxy nanocomposites and showed that for silica particles there was a significant decrease of around 30 K for the nanocomposites compared to the unfilled epoxy, citing residual organics and bonded water assisting molecular motions and creating additional free volume at the resin-filler interface [61]. Piscitelli et al. [20] showed a large reduction (~25 K) in T_g for an epoxy PNC with silica nanoparticles. The reduction in T_g was observed for 3 wt.% SiO$_2$ and was attributed to a plasticizing effect [62]. Piscitelli assigned the plasticizing effect to arise from the siloxane component entering the epoxy network and forming epoxy-siloxane

sequences [20], thereby increasing the distance between the epoxy units. Relating this to HNT, where siloxane groups are present on the surface of the nanofillers, the depression of 30 K seen at 12 wt.% can be assigned to a plasticizing effect as well. Here, the HNT surface is similar but not identical to that of SiO_2 discussed in [20]. Therefore, the strong reduction of the T_g value observed for Ep/HNT12 cannot be unambiguously assigned to the plasticizing effect of the external siloxane groups, although it is possible that such a mechanism can contribute to the decrease of T_g. Another important factor is the large aspect ratio of tubular nanofillers, which can significantly affect the curing reaction and thus the crosslinking density, especially for higher NPs concentrations.

(2) The second mechanism, the immobilization of segments due to the nanofiller, can be discussed in the frame of two scenarios. On the one hand, an immobilized fraction can be formed, the rigid amorphous fraction, where polymer segments are adsorbed on the surface of the nanofiller and therefore do not contribute to the cooperative segmental mobility increasing the glass transition temperature values. On the other hand, for a tubular nanofiller with a high aspect ratio, a percolation effect should be considered. A bridged network between the nanofiller and epoxy matrix can be formed for higher nanofiller concentrations, which restricts the segmental fluctuations of the system resulting in an increase in T_g. Ye et al. [37] reported that, for 2.3 wt.% HNT in an epoxy, the dispersion of HNT resulted in a two-phase structure. One phase consisted of HNT nanotubes homogenously dispersed with large inter-tube distances, forming an epoxy-rich region. In the second phase some of the halloysite nanotubes were dispersed with a short inter-tube distance resulting in an HNT-rich region. TEM images revealed that the spaces among the HNTs in this region were filled with epoxy. Ye et al. referred to this region as high content HNT embedded in a continuous matrix phase. For higher HNT concentration, this effect might become more pronounced, as more HNT are embedded in the continuous phase. The epoxy-matrix in this region will be exposed to additional confinement effects due to the short inter-tube distances. This assumption is confirmed by the TEM image for Ep/HNT15, given in Figure 4a, where the nanofillers are clustered together with some epoxy in between. Due to the additional confinement in this HNT-rich region, the polymer segments might be restricted in the cooperative segmental mobility, increasing T_g. Considering that the increase of T_g is found for the highest concentration of HNT, Ep/HNT15, this can be considered a critical concentration, where additional confinement in the HNT-rich regions of the PNC affects the overall segmental mobility of the whole matrix.

3.1.4. Specific Heat Spectroscopy

In addition to the information about the vitrification of the system, the segmental dynamics can be revealed using TMDSC. Specific heat capacity is a measure of the segmental mobility related to the glass transition of the samples. The modulus of the complex specific heat shows a step at the glass transition, similar to the heat flow curves from DSC. The step in the heat capacity was analyzed using the sigmoidal fit and derivative method to obtain the frequency dependent glass transition temperatures $T_{max,\alpha}$. As shown in Figure 5b as an example, the composition dependence of $T_{max,\alpha}$ at f = 0.0083 Hz has the same dependence as the T_g obtained from the two static techniques, further confirming the complex concentration dependence of the glass transition temperature for this system.

Interfacial Properties

Moreover, the modulus of the complex specific heat can be used to quantify both the mobile and rigid amorphous fractions with respect to the cooperative segmental motions. This analysis is based on the estimation of the step height of the specific heat capacity at the glass transition, denoted as the calorimetric strength Δc_p. For a PNC, Δc_p is expected to decrease compared to the unfilled material in the case that an immobilized interface is formed. In the three-phase model of a PNC, an amorphous nanocomposite is composed of mobile fraction (MAF), a possible RAF and the nanofiller. It should be noted that this

concept was initially introduced by Wunderlich for semicrystalline polymers and further extended to polymer-based nanocomposites [63]. MAF and RAF can be calculated by

$$MAF = \frac{\Delta c_{p,PNC}}{\Delta c_{p,\ pure\ epoxy}} \tag{2a}$$

$$RAF = 1 - filler\ content - MAF \tag{2b}$$

For epoxy-based nanocomposites, mobilization and immobilization effects can occur simultaneously, as discussed in [16], where the calorimetric strength was found to initially increase, reaching values higher for the nanocomposite than for the pure epoxy, followed by a subsequent decrease of Δc_p.

Figure 6a depicts the calorimetric strength at f = 0.0083 Hz as function of the nominal HNT concentration. The observed dependence can be divided in three different parts. In the first part (I) for concentrations between 0 and 6 wt.% HNT, Δc_p decreases with increasing filler concentration. This decrease means that the number of mobile segments decreases and thus the dominating effect is a formation of RAF. The amount of RAF increases with increasing concentration, as shown in Figure 6b, reaching up to 4% wt.% RAF for 6 wt.% HNT.
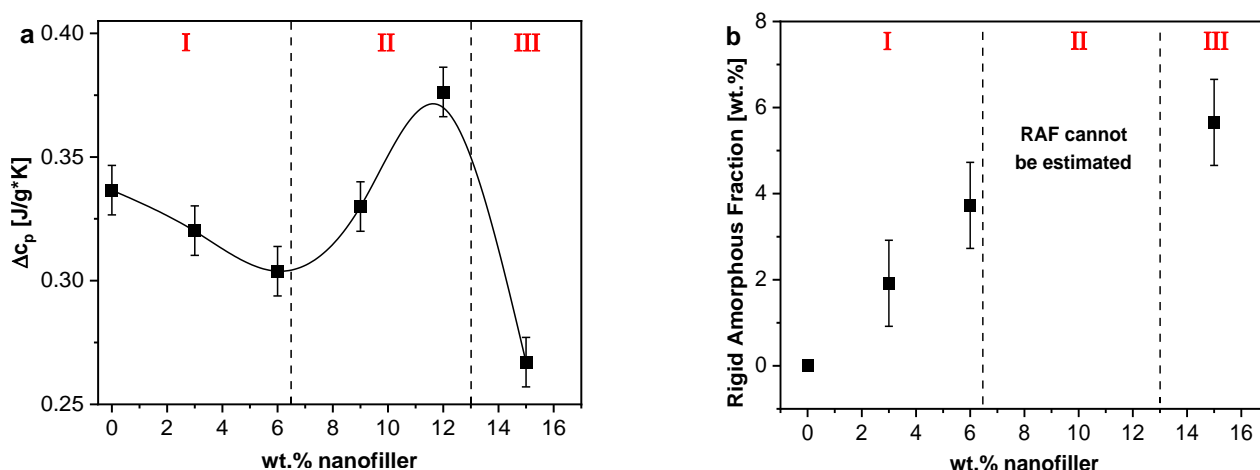

Figure 6. (**a**) The calorimetric strength, Δc_p; and (**b**) the calculated RAF as a function of filler content. Error bars are included. In (**a**), the line is a guide to the eyes.

In the next part (II) between 6 and 12 wt.% of HNT, an increase in Δc_p is observed reaching values higher than those observed for the unfilled epoxy. This means the dominating effect is a mobilization and hence the number of mobile segments is increased in comparison to unfilled epoxy. This can be attributed to a filler-related decrease in the crosslinking density as discussed above. This is in agreement with the decrease of T_g observed for 12 wt.% HNT. For all PNC samples, an immobilization and mobilization take place simultaneously; however, through TMDSC, the dominating effect is accessible. Therefore, in the first part (I), the decrease in the crosslinking density also occurs, but it is dominated by the formation of RAF. In the second part (II), the formation of RAF probably also takes place but is strongly overlaid by an increase of the number of mobile segments in the matrix. In contrast to previous observations, for flake-shaped Boehmite nanoparticles (BNP) in an anhydride-cured DGEBA epoxy matrix [27], where the increase in the number of mobile segments was observed for 1 wt.% of BNP followed by a consistent decrease of Δc_p with increasing BNP content, indicating an immobilization of segments. Here, the system under investigation is reinforced with nanofillers with different dimensions. The nanofiller has the form of a nanotube with a length > 400 nm compared to BNP with a primary diameter of ~14 nm. Consequently, the nanotubes impose more restrictions to the crosslinking reaction at higher concentrations compared to other shaped NPs dis-

cussed in the literature [64]. If one tried to calculate RAF for HNT concentrations between 6 and 12 wt.% HNT, negative values would be obtained. Since negative values of RAF contradicts its definition, this consideration indicates that the formation of RAF is strongly overlaid by the creation of mobile segments due to a decrease in crosslinking density. In other words, the latter process strongly dominates over the formation of RAF.

In the last part (III) for HNT concentrations between 12 and 15 wt.%, a sharp decrease of Δc_P is observed. Hence, the formation of RAF becomes again the dominant effect, which results in an effective value of RAF about 5 wt.%. As suggested by the increase of T_g in this concentration region, an additional reason for the increase of RAF might be related to the existence of an interconnected pathway of the polymer segments (percolating network). This behavior becomes more relevant at this nanofiller concentration [65], influencing the overall number of mobile segments by introducing additional confinements to the segmental fluctuations. This additional confinement might be due to the bridged network formed between the polymer and the nanofiller in the HNT-rich region.

In addition, temperature modulated fast scanning calorimetry was carried out to extend the investigation of the segmental dynamics by calorimetry in a broader frequency and temperature range. The combined calorimetric activation plot, where the logarithm of the relaxation rate is plotted as a function of inverse temperature, is depicted in Figure 7. The temperature dependence of the relaxation rates is curved in such a representation as expected for the dynamic glass transition. The Vogel–Fulcher–Tammann [66–68] (VFT) equation was employed to describe the temperature dependence of the relaxation rates. The VFT equation is given by

$$f_{p,\alpha}(T) = \frac{1}{2\pi\tau(T)} = f_\infty \exp\left(\frac{-DT_0}{T - T_0}\right). \tag{3}$$
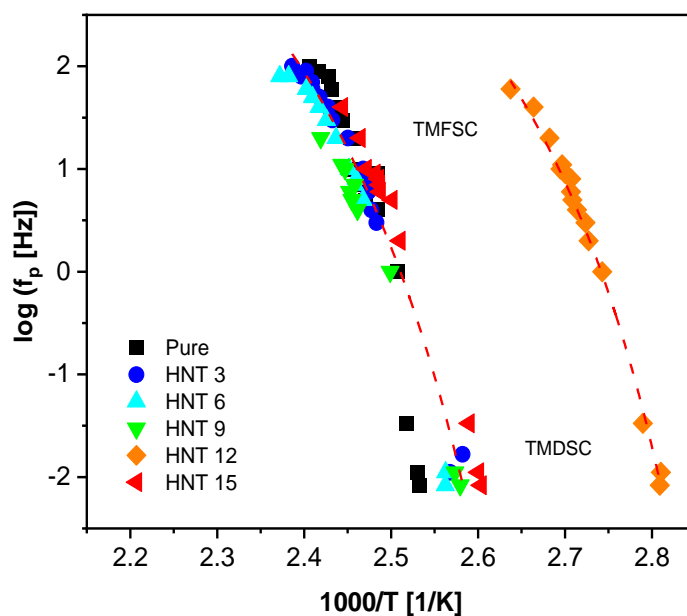

Figure 7. Combined calorimetric activation plot for TMFSC and TMDSC: black squares, pure epoxy; blue circles, Ep/HNT3; teal triangles, Ep/HNT6; green triangles, Ep/HNT9; orange diamonds, Ep/HNT12; red triangles, Ep/HNT15. The red lines are exemplary VFT fits to the data of Ep/HNT3 and Ep/HNT12.

f_∞ is a pre-exponential factor ($f_\infty \approx 10^{10}$–10^{12} Hz); T_0 is the Vogel temperature or ideal glass transition temperature, which is found 20–40 K below the thermal glass transition temperature; and D is the fragility parameter that is used to quantify glass forming systems. The VFT fit lines are included in Figure 7, and the data obtained from the two frequency

dependent techniques can be described by the same fits. The temperature modulated calorimetric relaxation data are further discussed when compared to the results obtained from BDS.

3.1.5. Broadband Dielectric Spectroscopy

The dielectric loss as function of frequency and temperature for the pure epoxy and 15 wt.% HNT is depicted as 3D representations in Figure 8. Three dielectric processes are identified in both 3D plots. One process is the segmental relaxation labeled as α-relaxation which is active at temperatures above the glass transition temperature. This process is related to cooperative segmental fluctuations within the epoxy network. It is hidden by a large increase in dielectric loss due to conductivity and polarization effects arising from the migration and/or blocking of charge carriers which are due to remaining ion impurities. This feature is considered as a parasitic effect and is not relevant to the scope of this work [28]. Further, at lower temperatures than relevant for the α-relaxation, a broad relaxation process is found, assigned to the local molecular fluctuations such as the β-relaxation.
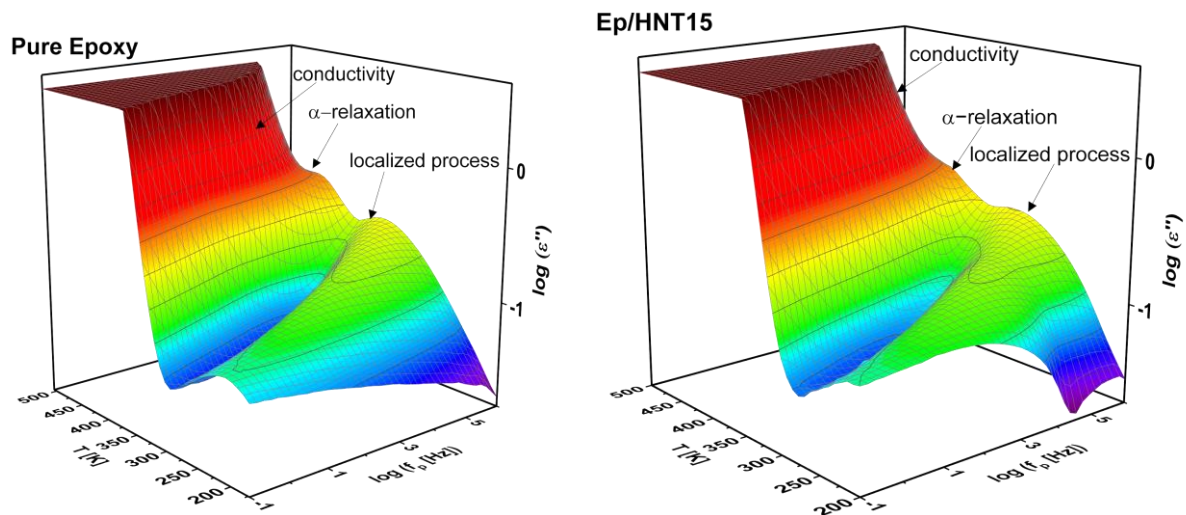

Figure 8. Three-dimensional plots of dielectric loss as a function of frequency and temperature for pure epoxy and the nanocomposite with 15 wt.% HNT.

For a more detailed discussion of the dielectric behavior, the dielectric loss is plotted in Figure 9 as a function of temperature (isochronal representation) at $f = 10^3$ Hz for the pure epoxy and Ep/HNT6 and Ep/HNT15. Similar to the 3D plots, three well pronounced dielectrically active features can be identified. However, in Figure 9, an additional low-temperature relaxation process can be observed as a low intensity shoulder of the β-relaxation, denoted as γ-relaxation.
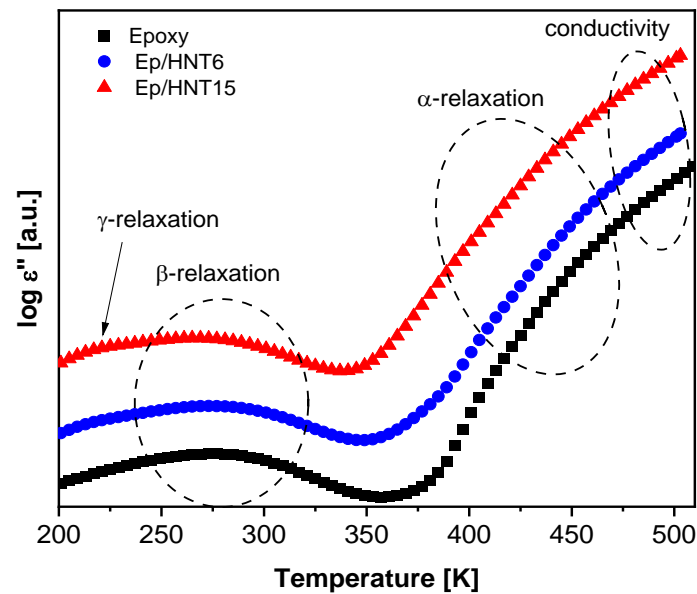
Figure 9. Dielectric loss spectra at a frequency of 1000 Hz for selected samples. Black squares, unfilled epoxy; blue circles, Ep/HNT6; red triangles, Ep/HNT15. The dielectric loss is shifted along the *y*-axis for sake of clarity.

Localized Molecular Fluctuations

Dielectric loss data are commonly analyzed in the frequency domain (isothermal) by fitting the Havriliak–Negami (*HN*) function [69,70] to the dielectric loss plots. The HN function reads

$$\varepsilon^*_{HN}(\omega) = \varepsilon_\infty + \frac{\Delta\varepsilon}{\left(1 + (i\omega\tau_{HN})^\beta\right)^\gamma} \tag{4}$$

where $\Delta\varepsilon$ is the dielectric strength, $\varepsilon_\infty = \lim_{\omega\to\infty} \varepsilon'(\omega)$ and τ_{HN} is the characteristic relaxation time. β and γ are fractional shape parameters ($0 < \beta \leq 1$ and $0 < \beta\gamma \leq 1$) that describe the broadening and asymmetry of the peak, respectively. The relaxation rate (f_p) is then obtained as the frequency of the peak maximum position of the dielectric loss using the obtained fitting parameters. An example of the HN fit to the data for Ep/HNT3 at 298 K is shown in Figure 10a. In accordance with the 3D plots, at 289 K, one dielectrically active process is found, denoted as β-relaxation. The molecular origin of this relaxation has been discussed previously [57,71–73], with the β-relaxation being assigned to the crankshaft motions of small fragments of segments between crosslinks [74]. However, in another approach, this relaxation was associated with the localized motions of dipoles formed during the crosslinking reactions (hydroxyl ether and secondary or tertiary amine groups) [75]. Ochi et al. proposed that it was the sum of the contributions from the hydroxyether group for bisphenol-A-type epoxide resins cured with aliphatic amines [72]. It has also been discussed that the β-relaxation arises from the local motions of dipoles of unreacted components during curing, specifically epoxide rings [73]. Recent findings for a similar amine-cured system employing low field proton nuclear magnetic resonance (NMR) spectroscopy [11] reveal that, due to the significant amplitude of proton motions, β-relaxation is probably associated with the rotational motions of para-substituted phenyl rings of DGEBA, i.e., phenyl rings with the adjacent ether linkages.
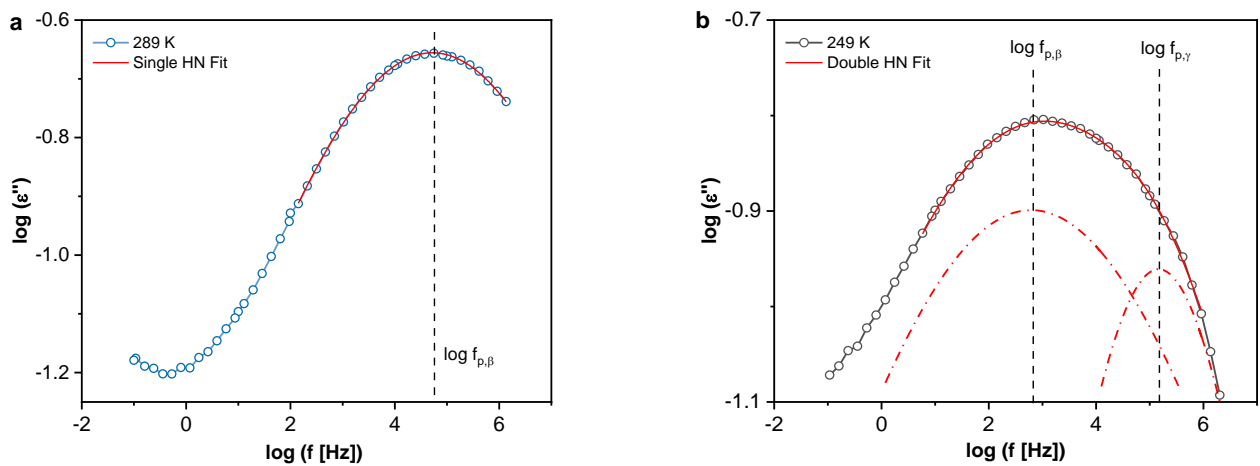
Figure 10. (**a**) Single HN function fit; and (**b**) double HN function fit with the labeled relaxation rates for Ep/HNT3.

Furthermore, as previously discussed, at temperatures below approximately 280 K, a second low intensity shoulder emerges at high frequencies compared to the β-relaxation, denoted as γ-relaxation. A sum of two HN functions were then fitted to the data and two characteristic relaxation times were determined. Figure 10b shows the fit of the two HN functions as example and the positions of the β- and γ-relaxations. The γ-relaxation is a low intensity process related to groups with either a weaker dipole moment or a lower number density of fluctuating dipoles involved in this process. In addition, this process is more pronounced for the PNCs than for the pure epoxy, increasing in intensity with increasing HNT content. For higher concentrations of NPs epoxy networks tend to be more heterogeneous, having for instance more "dangling ends" (unreacted end groups of the resin/hardener). Therefore, it can be assumed that the γ-relaxation is related to the local motions of those dipoles that remain as the unreacted components during curing (see Figure 9).

The logarithm of the relaxation rates as a function of inverse temperature were plotted into a relaxation map, as given in Figure 11a. Both processes for the pure epoxy and the PNCs follow the Arrhenius equation (Equation (5)), as typical for localized processes.

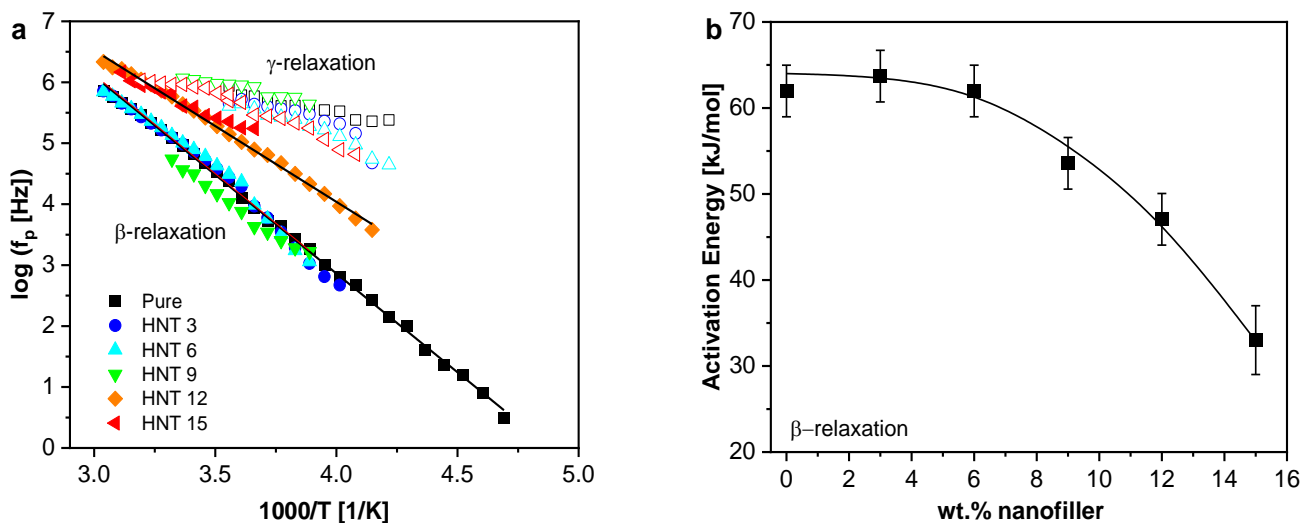$$\log f_p = f_\infty \exp\left[\frac{-E_A}{RT}\right]. \tag{5}$$

Figure 11. (**a**) Activation plot for the β-relaxation (solid symbols) and γ-relaxation (open symbols). Black squares, pure epoxy; blue circles, Ep/HNT3; teal triangles, Ep/HNT6; green triangles, Ep/HNT9; orange diamonds, Ep/HNT12; red triangles, Ep/HNT15. Black lines are Arrhenius fits to the data. (**b**) The activation energy for the β-relaxation as a function of the HNT concentration.

Here, f_∞ is the relaxation rate at infinite temperatures, E_A is the activation energy and R is the ideal gas constant. As stated above, the γ-relaxation is seen as a low intensity shoulder of the β-relaxation, therefore the dependence of the intensity on the concertation of the nanofiller cannot be quantitatively addressed. Because of the scatter in the relaxation rates, only an averaged activation energy E_A of ca. 28 kJ mol^{-1} can be given. The errors for the activation energy here are below 3 and 4 kJ mol^{-1} for the highest nanofiller concentration. In Figure 11b, the estimated activation energies for the β-relaxation are plotted versus the concentration of HNT. E_A decreases systematically from 65 to 29 kJ mol^{-1} with increasing nanofiller concentration. To discuss this finding, it should be noted that the crosslinking density depends on the nanofiller content and lower crosslinking densities are expected for higher nanofiller contents. Therefore, the free volume in the system might increase, leading to a decrease of the activation energy. The decrease of the activation energy for the PNCs compared to the pure epoxy also confirms the theory suggested by Hassan et al. [75] that the β-relaxation is sensitive to differences in the distribution of local free volume, related to the different crosslinking density. Hassan et al. studied two bisphenol-A based epoxies cured with different crosslinking agents. The position of the β-relaxation peak for both systems differs due to different crosslinking densities of the samples. Additionally, in a free volume study by positron annihilation lifetime spectroscopy (PALS) performed by Patil et al. [76] for bisphenol-A resins cured with different curing agents, the epoxies with a lower crosslinking density had a higher free volume. The activation energies for these epoxies were also estimated where the samples with the higher free volume showed a lower activation energy.

Segmental Dynamics

As discussed above, the segmental dynamics (α-relaxation) of the system is hidden by conductivity. Therefore, to minimize this contribution, a conduction-free analysis [77] was carried out. The real part of the complex dielectric function ε' was differentiated with respect to frequency. For the Debye function, this approach results in: (I) a peak appearing in the derivative of ε' named ε''_{deriv}; (II) due to the square, the peak becomes narrower than the peak observed for ε'' (see Equation (6)); and (III) the Ohmic conductivity contribution ($\varepsilon'' \sim 1/\omega$) is removed because ε' is independent of frequency for that case.

$$\varepsilon''_{deriv} = -\frac{\partial \varepsilon'(\omega)}{\partial \ln \omega} \sim (\varepsilon'')^2 \tag{6}$$

For the HN function, the derivative of the real part is calculated as

$$\frac{\partial \varepsilon'_{HN}}{\partial \ln \omega} = -\frac{\beta \gamma \Delta \varepsilon_{HN} (\omega \tau_{HN})^\beta \cos\left(\frac{\beta \pi}{2}\right)(-(1+\gamma)\Psi(\omega))}{\left[1 + 2(\omega \tau_{HN})^\beta \cos\left(\frac{\beta \pi}{2}\right) + (\omega \tau_{HN})^{2\beta}\right]^{\frac{1+\gamma}{2}}} \tag{7}$$

where $\Psi(\omega)$ is

$$\Psi(\omega) = \arctan\left[\frac{\sin\left(\frac{\beta \pi}{2}\right)}{(\omega \tau_{HN})^{-\beta} + \cos\left(\frac{\beta \pi}{2}\right)}\right] \tag{8}$$

The isothermal scans of the α-relaxation were analyzed by fitting $\frac{\partial \varepsilon'_{HN}}{\partial \ln \omega}$ to the derivative of ε' and the relaxation rates for the α-relaxation were extracted (Figure 12a). The data can also be analyzed in the temperature domain (TD) at a fixed frequency (isochronal scans), where an additional relaxation process to the α-relaxation was observed, denoted as α*-relaxation. The peak maxima location was obtained employing a Gaussian fit to these data. However, a Lorentzian function or a parabola could also be used to analyze the isochronal data. The relaxation map for these two relaxation processes (Figure S10) illustrates that the temperature dependence of the relaxation rates of the α*-relaxation (temperature domain, isochronal representation) deviates strongly from that of the α-relaxation

(frequency domain, isothermal scans). This result indicates the different molecular origins of both processes. These two processes were found at temperatures above the calorimetric glass transition region (at high frequencies). For other nanocomposite systems, an additional relaxation process related to some molecular mobility of the RAF has been previously discussed [12,78,79]. Through BDS, it was shown that RAF is not completely immobile, and a localized relaxation process can be found, faster than the bulk relaxation process with an Arrhenius-like temperature dependence. However, this cannot be the origin for either the α*-relaxation or the α-relaxation because this relaxation process was also observed for the pure epoxy. The presence of two segmental relaxations (two dynamic glass transitions) was observed by some authors [27,28] for epoxy-based systems. These processes were assigned to the structural heterogeneity of the epoxy-based matrix. Regions with lower crosslinking density would have a weaker temperature dependence compared to regions with a higher crosslinking density. Thus, α*-process was assigned to these regions. Accordingly, the α-relaxation is then linked with regions with higher crosslinking density.
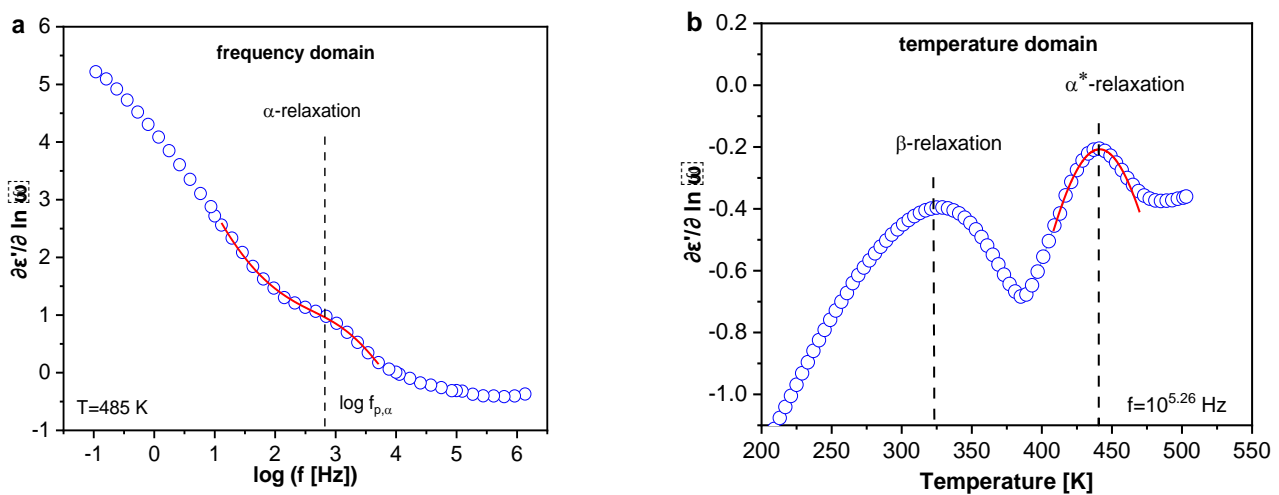

Figure 12. (**a**) Analysis of the α-relaxation in the frequency domain using $\frac{\partial \varepsilon'(\omega)}{\partial \ln \omega}$ at T = 485 K, where the red line indicates the $\frac{\partial \varepsilon'_{HN}}{\partial \ln \omega}$ fit; and (**b**) analysis in the temperature domain using $\frac{\partial \varepsilon'(\omega)}{\partial \ln \omega}$ at f = $10^{5.26}$ Hz, where the red line is the Gauss fit to the curve.

To obtain a better understanding of the segmental fluctuations, the calorimetric relaxation data were added to the dielectric data. Interestingly, the TMDSC, TMFSC and α*-relaxation data have the same temperature dependence of their relaxation rates and can be described by one VFT function. This agreement indicates that the two calorimetric techniques and the isochronal scans (temperature domain) of BDS probe the same process. The process found in the frequency domain of BDS does not follow this dependency, meaning that the α-relaxation was not detected by TMDSC and TMFSC. However, as suggested in [29], the relaxation rates of the α-process can be directly compared to the thermal relaxation data estimated from the static thermal measurements. Therefore, FSC measurements at different heating rates (10^2–10^4 K s^{-1}) were performed on the samples. Similar to conventional DSC, the step in the heat flow curves was fitted with a sigmoidal function. Next, the fit function was differentiated with respect to temperature and T_g was taken as the maxima of the resulting peak. The heating rate from the static FSC data can be transformed to a thermal relaxation rate the frame of the fluctuation model of Donth [80] by

$$f_p = C \frac{\dot{T}}{2\pi \Delta T_g} \tag{9}$$

C is a constant with a value close to one, $\dot{T}$ is the heating rate and ΔT_g is the width of the glass transition. The width of the glass transition was taken as the difference between

the onset and end set of the glass transition. In addition, according to the fluctuation approach, the square root of $\Delta T_g^{1/2}$ should be linearly dependent on the glass transition temperature [81]; therefore, a linear regression line was fit to the data (Figure S11). From the regression line, the averaged ΔT_g values were calculated and taken for each glass transition temperature and used in Equation (9) to reduce the scattering [28]. A combined relaxation map of the dielectric data and all calorimetry data is given in Figure 13, for the pure epoxy and 3 and 15 wt.% HNT. This figure shows that dielectric data obtained from the isothermal analysis agree in their temperature dependence with the relaxation rates obtained by FSC. As stated above, one VFT fit was used for the data of the α^*-relaxation and the SHS data. The static FSC data do not follow the temperature dependence of the other calorimetric relaxation rates. One VFT fit was used for the thermal relaxation rates from the static FSC and the dielectric α-relaxation, indicating that they have the same molecular origin. A similar behavior was observed for an Epoxy/LDH nanocomposite system [29]. Interestingly, the static FSC data curves at lower frequencies seem to show a crossover behavior from the α-process at higher frequencies (higher temperatures) to the α^*-process at lower frequencies (lower temperatures). This crossover behavior might indicate that in the static calorimetric measurements the material response for the considered system is always due to the slower process (lower relaxation rate at a given temperature).
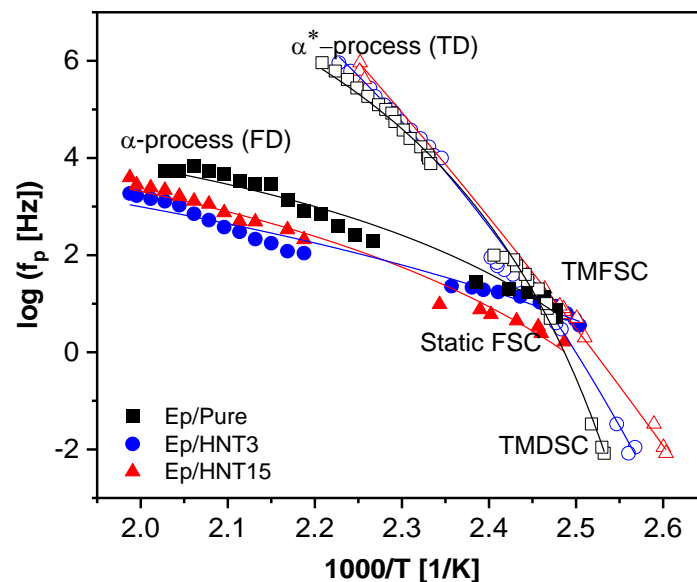

Figure 13. Combined map for pure epoxy and nanocomposites (Ep/HNT3 and Ep/HNT15). The lines are VFT fits to the different data sets.

3.2. Epoxy Nanocomposite with Modified Halloysite Nanotubes (Ep/m-HNT)

The HNT were modified with PDA and ultrafine iron nanodots to improve the interactions with the epoxy [36]. The hydroxyl groups of PDA might allow for a better interaction with the matrix by forming hydrogen bonds with the epoxide groups of the DGEBA. The m-HNT nanocomposites were investigated with a focus on the structure, molecular mobility and vitrification of this system in comparison to the nanocomposite with unmodified HNT in order to understand the effect of the surface modification.

3.2.1. X-ray Scattering

As for the unmodified HNT and corresponding PNCs, the structure of the modified filler and morphology of the related nanocomposites was investigated using X-ray scattering, as discussed above. As shown for m-HNT in Figure S12, in comparison to unmodified HNT, the crystal structure of the filler was not affected by the modification. Moreover, for Ep/m-HNT6 and Ep/m-HNT15, the scattering pattern in the WAXS region of the matrix (broad peaks related to carbon–carbon correlations) resembles that of the

PNCs reinforced with unmodified HNT. This indicates that X-ray scattering does not detect differences in the matrix structure, compared to Ep/HNT, related to the nanofiller modification. The main difference between HNT and m-HNT is the larger outer diameter of the cylinder (D_{outer}) of 113 nm for m-HNT in comparison to 107 nm for the HNT. The increase of D_{outer} for the modified particles is due to an additional layer of PDA on the external particle surface. From the difference of the two values, one can conclude that the thickness of the PDA layer is about 3 nm. Similar to Ep/HNT, for the two PNCs (Ep/m-HNT6 and Ep/m-HNT15), the D_{outer} of m-HNT increases when embedded in the matrix, compared to the pure particles (113 nm, m-HNT; ~126.7 nm, PNCs). However, for Ep/m-HNT, the increase of D_{outer} is smaller than for Ep/HNT because the PDA coating partially prevents the intercalation of small molecules into the cylinder rolls.

3.2.2. TEM

A TEM image for the sample Ep/m-HNT15 is given in Figure 14 as an example. Although some clusters still exist in the nanocomposites, the m-HNT nanofillers are better dispersed compared to the nanocomposites containing the unmodified HNT (see Figure 4). This is observed for all concentrations of m-HNT.
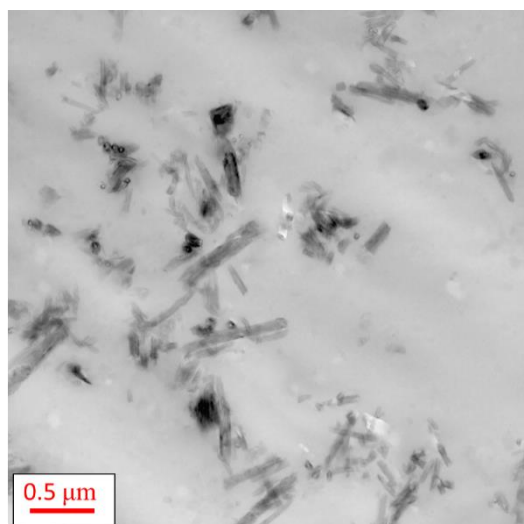

Figure 14. TEM image for Ep/m-HNT15 at a magnification of 0.5 µm.

3.2.3. Calorimetry

The estimated T_g values by DSC show a non-monotonous concentration dependence (see Figure 15). Nevertheless, in comparison to the Ep/HNT system, for the m-HNT containing system, the glass transition temperature values for the nanocomposites do not decrease compared to that of the pure epoxy. For three concentrations of m-HNT (6, 9 and 15 wt.%), the T_g values are similar to the pure epoxy, whereas, for 3 and 12 wt.%, T_g is ca. 8 K higher than that of the pure epoxy. This behavior is not easy to understand. As for the unmodified system, a competition between mobilization of the segments due to the nanofiller-related changes in crosslinking density and immobilization related to an interphase formation is expected. Different from the Ep/HNT system, a siloxane-related plasticization effect is not relevant for this system, due to the surface modification. Moreover, the immobilization effect of the segments at the filler–matrix interface is expected to be stronger because of a possible formation of hydrogen bonds between the PDA amine hydroxyl groups and the hydroxyl groups of the epoxy [82,83]. The immobilization might be counterbalanced by a mobilization effect due to a decrease in the crosslinking density related to the incorporation of nanofillers. This would result in a T_g value which is similar to that of the pure epoxy. The increase of the T_g for 12 wt.% of m-HNT might be discussed by a kind of percolation of the RAF phase which has a maximum for 12 wt.% (see below).

For 15 wt.% m-HNT, this percolation effect is overcompensated by a further decrease in the crosslinking density. In addition, since the surface modification results in a better dispersion of the nanofillers in the epoxy matrix, there exists less amount of an HNT-rich phase, as expected for the unmodified system. Thereby, the discussion applied for the HNT embedded in a continuous matrix phase described for Ep/HNT15 would not be applicable for higher nanofiller content for the m-HNT samples. This is shown in Figure 15, where for Ep/m-HNT15 the T_g is comparable to the unfilled epoxy value.
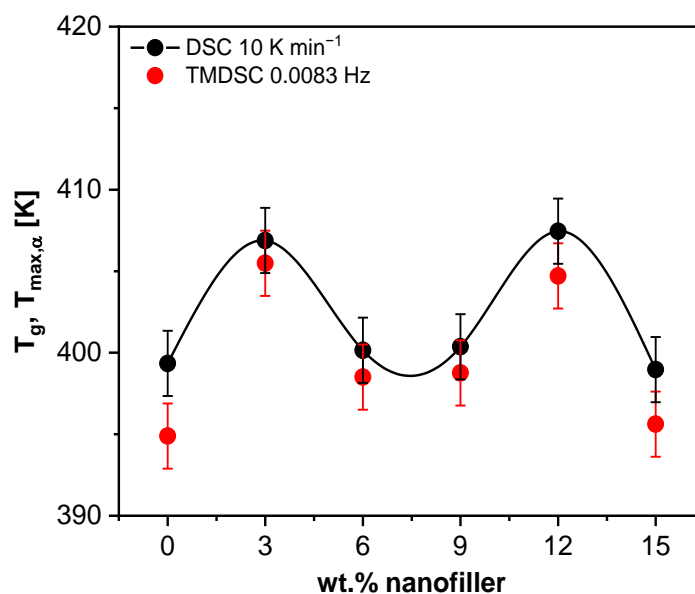

Figure 15. Glass transition temperature as a function of m-HNT content estimated by DSC and TMDSC. The line is a guide to the eyes.

3.2.4. Specific Heat Spectroscopy

The reversing specific heat capacity obtained from TMDSC was used to calculate the frequency dependent glass transition temperature, $T_{max,\alpha}$, plotted as a function of filler content in Figure 15 at f = 0.0083 Hz. The $T_{max,\alpha}$ values show a similar non-monotonous concentration dependence as the DSC data.

Interfacial Properties

In addition, from the reversing specific heat capacity, the calorimetric strength and amount of RAF were determined as described above. Both Δc_p and RAF are depicted as a function of m-HNT content in Figure 16. The Δc_p decreases systematically with increasing nanofiller content. The immobilization of segments by the nanofillers due to interface formation is the dominant effect for all concentrations of the nanofiller resulting in a decreased calorimetric strength. This behavior is confirmed as the amount of RAF increases and reaches a maximum value at ca. 12 wt.% m-HNT. The observed maximum can be taken as an indication that agglomerates are formed in the system, as discussed for an epoxy filled with Boehmite [27]. This would reduce the amount of interfacial area available for RAF formation, compared to the dispersed nanofillers. For comparison, the data for the system containing the unmodified nanofiller is included in Figure 16. This comparison demonstrates the different behavior of both nanocomposites systems. The amount of RAF formed for Ep/m-HNT is essentially higher than that of Ep/HNT. The concentration dependence of RAF for Ep/m-HNT increases for all concentration of m-HNT, indicating a significant interphase formation. The different RAF formation for both systems is also reflected in the different concentration dependence of Δc_p. However, the application of the three-phase model is limited because the reduction in crosslinking density is not taken into account. Therefore, only lower limits of RAF can be estimated.
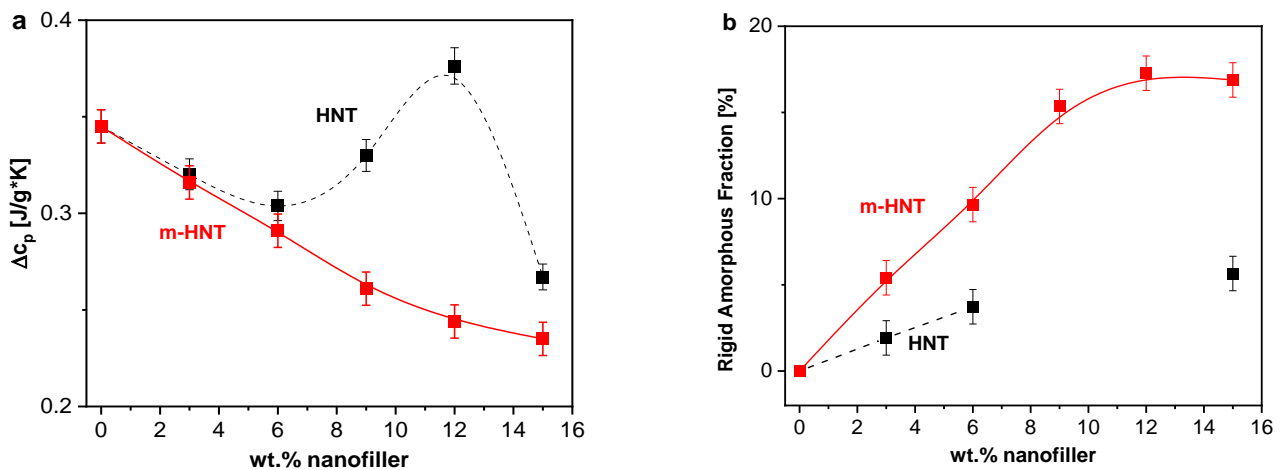
Figure 16. (**a**) Δc_p and (**b**) RAF as function of the filler content for m-HNT (red) and HNT (black). Line are guides for the eyes.

Segmental Dynamics

The relaxation rates from TMDSC and TMFSC were also estimated as for the unmodified HNT system and plotted in the activation plot (Figure S15). A similar temperature dependence as for the unmodified system was observed for both methods. The data can be described by one VFT function for each sample. The calorimetric techniques probe the relaxation processes related to entropy fluctuations. Thereby, the relaxation plots were further extended with data from BDS to gain a complete picture of the segmental dynamics.

3.2.5. Broadband Dielectric Spectroscopy

BDS was employed to study the molecular mobility of the m-HNT PNCs similar to the unmodified HNT. 3D dielectric loss spectra for the samples with 6 and 15 wt.% m-HNT are depicted in Figure 17. The segmental relaxation (α-relaxation), localized fluctuations (β-relaxation) and conductivity contribution were observed to be similar to Ep/HNT. The found relaxation processes were analyzed analogously to that for the pure and Ep/HNT samples. As stated above, conductivity is a parasitic effect and is be further addressed.
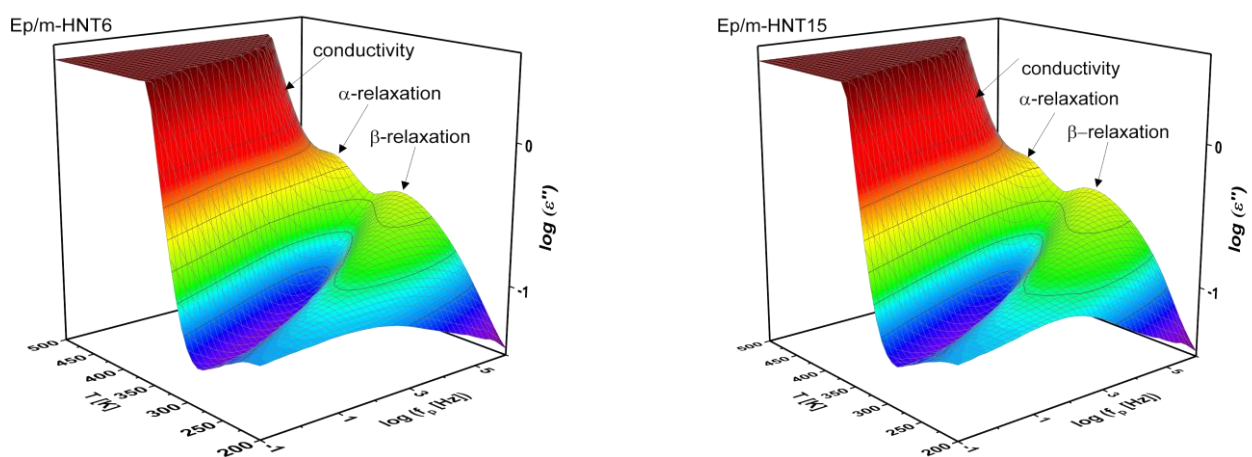

Figure 17. 3D plots of the dielectric loss spectra as a function of frequency and temperature for Ep/m-HNT6 and Ep/m-HNT15.

The isochronal data for Ep/m-HNT15 was plotted alongside the pure epoxy and Ep/HNT15 sample in Figure 18 for a direct comparison of both systems. Similar to the unmodified system, the γ-processes is more pronounced for Ep/m-HNT15 than for pure epoxy, due to more dangling ends (unreacted end groups) in the matrix. Further, the β- and α-process are observed at similar positions for all samples, however a more detailed

discussion is given below. The interfacial polarization effects polarizations effects seem to be more pronounced for Ep/m-HNT compared to Ep/HNT. Due to the better dispersion of the nanofiller more surface is available for the blocking of charges.
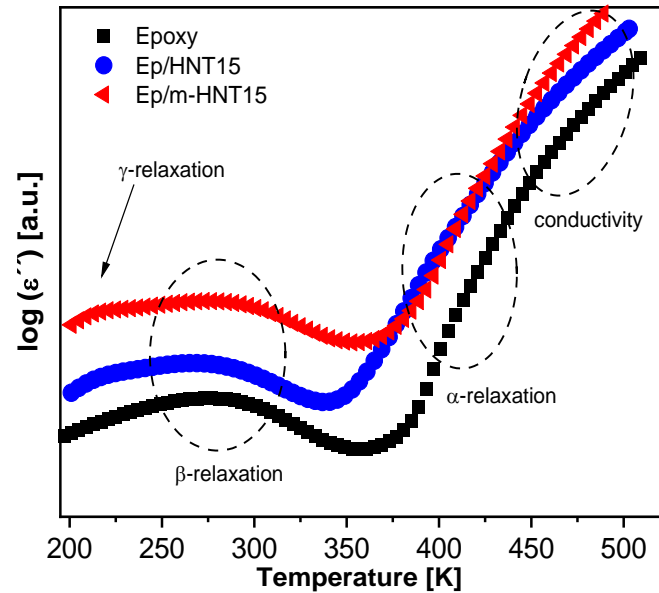

Figure 18. Dielectric loss spectra at a frequency of 1000 Hz for selected samples. Black squares, Ep/Pure; blue circles, Ep/HNT15; red triangles, Ep/m-HNT15.

Localized Molecular Fluctuations

As discussed for the system with the unmodified nanofiller, the β-relaxation can be analyzed by fitting a single HN function to the data at higher temperatures, where at lower temperatures the low intensity γ-relaxation was observed, and there the data were fitted by the sum of two HN-functions.

The relaxation rate values were extracted and plotted in the relaxation map. The activation map for these local relaxation processes is plotted in Figure S17 and the estimated activation energy for the β-relaxation is depicted in Figure 19a. The m-HNT system shows a decrease of the activation energy but with a different concentration dependence compared to the HNT system. As discussed above for the unmodified HNT samples, the decrease in E_a is a result of an increase in free volume caused by the decrease in crosslinking density. The incorporation of nanofiller reduces the crosslinking density, resulting in a higher free volume. The different concentration dependence found for the activation energy of the β-relaxation also reflects the difference in the interaction of the two nanofillers with the epoxy matrix.
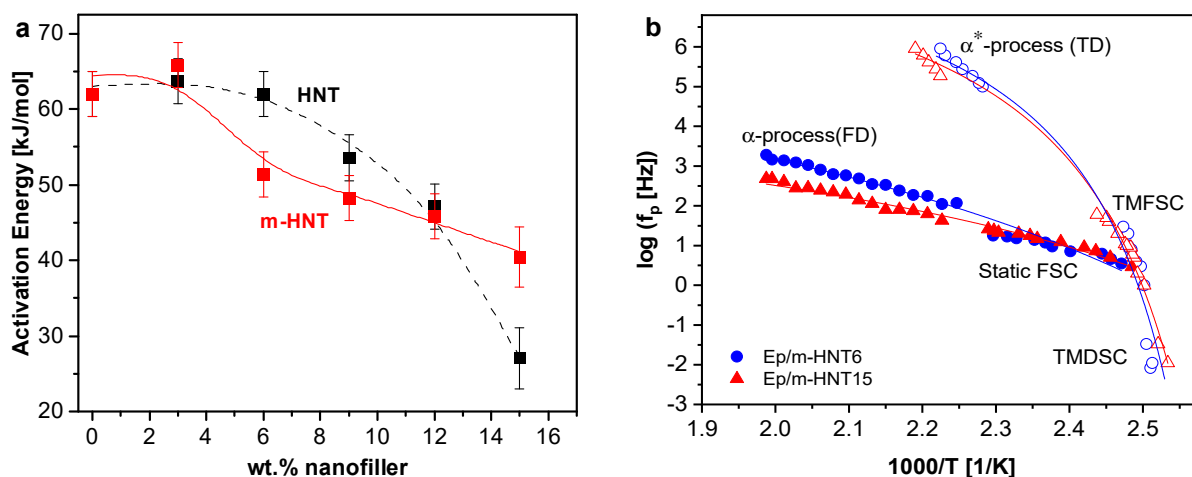
Figure 19. (**a**)The activation energy for β-relaxation as a function of wt.% m-HNT (red) and HNT (black). The lines are a guide to the eyes. (**b**) Combined relaxation map for 6 and 15 wt.% m-HNT. The lines are fits of the VFT equation to the corresponding data.

Segmental Dynamics

For the segmental dynamics, the conduction-free analysis was also employed as for the system with the unmodified filler. $\frac{\partial \varepsilon'_{HN}}{\partial \ln \omega}$ was used to analyze the α-relaxation in the frequency domain and the α*-relaxation in the isochronal domain (temperature domain). The activation map for both relaxations is shown in Figure S18, and, as for the unmodified system, the temperature dependence of the α*-relaxation deviates strongly from the α-relaxation, which indicated different molecular origins for both processes. For m-HNT, the combined α-relaxation plot with the results from the TMDSC, TMFSC, static FSC (fluctuation model, Equation (9)) and BDS is shown in Figure 19b. For clarity, only 6 and 15 wt.% m-HNT are plotted. Similar temperature dependencies are observed for the modified HNT system, compared to that of the modified samples. Again, one VFT function is used for the description of the dielectric α*-relaxation and the SHS data (TMDSC and TMFSC) and a second VFT fit for the α-relaxation and the thermal relaxation rates deduced from static FSC. As for the unmodified system, the two processes are assigned to the structural heterogeneity of the system. The regions with higher crosslinking density to the α-process and regions with lower crosslinking density to α*-process. The m-HNT system does not show a pronounced crossover at lower frequencies (lower temperatures) for the thermal relaxation rates.

4. Conclusions

In this study, epoxy nanocomposites, based on DGEBA cured with DETA with varying amounts of pristine and surface modified (PDA, iron nanodots) HNT nanofillers, were investigated for the first time using a combination of X-ray scattering, advanced calorimetry, specific heat and broadband dielectric spectroscopy. The morphology was first investigated by SAXS and WAXS. For the pure epoxy, three broad peaks in the WAXS region were found, related to the inherent spatial heterogeneity of the crosslinked network. A similar behavior was found for the nanocomposites. The SAXS data were analyzed using the Monte Carlo fitting method to obtain the size distributions of the nanofillers. The outer diameter of HNT and m-HNT was found to increase when embedded in the matrix, compared to the pure particles, due to the intercalation of resin and/or hardener in the cylinder rolls prior to the crosslinking reaction. The surface modification also resulted in a larger outer diameter of the filler by ca. 6 nm due to an additional layer of PDA on the external particle surface.

The glass transition behavior was elucidated using DSC measurements. For both HNT and m-HNT, the concentration dependence of the glass transition behavior was due to

two competing mechanisms: (I) the mobilization of the nanofiller due to the reduction of crosslinking density; and (II) the formation of an immobilized region at the filler–matrix interphase. For the HNT samples, two additional factors were also considered: mobilization of the matrix due to the plasticizing effect related to the siloxane groups of HNT and an immobilization effect for highly loaded samples due to the formation of HNT- and epoxy-rich regions. For the Ep/HNT system, the T_g for each concentration was found to be lower than for the pure epoxy, showing a decrease down to 12 wt.% due to the mobilization of the matrix being a dominant effect. For the highest concentration, an increase of T_g was observed due to the additional confinement on the matrix in the epoxy-rich region. On the contrary, for m-HNT no reduction of the glass transition temperature was observed, with higher T_g values for some concentrations, compared to that of the pure epoxy. This indicates that firstly no plasticization is present and secondly a stronger interaction between the matrix and the nanotubes is expected due to a hydrogen bonding between the hydroxyl groups of PDA with DGEBA. In addition, due to the stronger NP–matrix interaction, the m-HNTs are less agglomerated than HNTs, and, thus, immobilization due to the nanoparticle-rich region is not observed.

TMDSC was used to investigate the molecular mobility and structure, including the immobilized fraction at the matrix/particle interface (RAF) of the samples. For the unmodified HNT, the concentration dependence of the specific heat capacity showed that the discussed competition of mobilization and immobilization of the NPs led to both a decrease and an increase in the calculated values of calorimetric strength (Δc_p) compared to that of the pure epoxy. Above the concentration of 6 wt.% HNT, the three-phase model cannot be used to describe the interphase, as the mobilization of the matrix is the dominating effect. For Ep/m-HNT, the calorimetric strength decreases systematically with increasing filler content, indicating that the interphase formation was dominant over matrix mobilization for all concentrations. RAF showed a systematic increase with increasing NPs concentration and reached values up to ~16%. The higher RAF amounts for Ep/m-HNT compared to Ep/HNT are a result of the surface modification related to stronger matrix–NP interaction and more homogenous distribution of nanofillers in the epoxy matrix.

Further, the molecular mobility was studied using broadband dielectric spectroscopy. For both nanocomposites at temperatures below the T_g, β-relaxation and γ-relaxation were found and attributed to the rotational motions of the phenyl rings of DGEBA and the local motions of unreacted components, respectively. The activation energy was estimated for the β-relaxation, showing a decrease with increasing nanofiller content for both systems. The decrease in E_a is a result of an increase in free volume caused by the decrease in crosslinking density. At temperatures above the glass transition region, α-relaxation was found in the frequency domain (isothermal scans). An additional process was found in the temperature domain (isochronal scans) at high frequencies, named α*-process, which is also related to segmental dynamics. The presence of the two processes indicated a structural heterogeneity of epoxy-based materials, as implied by X-ray scattering. The two relaxations were assigned to regions in the matrix with different crosslinking density. The α*-process was assigned to regions with lower crosslinking density and the α-process to higher crosslinking density. The complete activation map was constructed by also including the calorimetric relaxation rates (TMDSC and TMFSC) and thermal relaxation rates calculated from static FSC measurements. Two different VFT functions were fitted, one for the TMDSC, TMFSC and dielectric α*-process (frequency domain) and the other for the static FSC and the dielectric α-process (temperature domain). Interestingly, thermal relaxations from static FSC show a crossover behavior for Ep/HNT from α-process at higher frequencies to α*-process at lower frequencies, not observed for the modified system.

0.5 and 1 nm), D_{lumen} (lumen size) (3, 5 and 7 nm), D_{length} (tube length) (50, 100 and 150 nm), and D_{outer} (outer diameter) (11.5, 13 and 16 nm) to show the fit changes with variations in length parameters. Figure S5: TEM images for Ep/HNT6 at lower magnification and higher magnification.; Figure S6: Heat flow curve for Ep/HNT3 with a heating rate of 10 K min^{-1}.; Figure S7: Flash DSC data for EP/HNT6 with various heating rates.; Figure S8: Modulus of the specific heat capacity $\left|c_p^*\right|$ for the Ep/HNT3 using an isotherm time of 120 s.; Figure S9: Normalized modulus of the heat capacity $\left|C_p^*\right|$ at 20 Hz for Ep/HNT nanocomposites and the pure epoxy.; Figure S10: Combined α-relaxation plot with the α- and α*-processes.; Figure S11: The square root of the glass transition width as a function of T_g.; Figure S12: X-ray scattering patterns of the pure epoxy, modified halloysite nanotubes and nanocomposites (Ep/m-HNT6 and Ep/m-HNT15).; Figure S13: Volume-weighted size distribution from Monte Carlo fitting methods for the Ep/m-HNT6 and Ep/m-HNT15 samples, as well as the m-HNT nanofiller.; Figure S14: Heat flow curves for the pure epoxy and the modified HNT samples at 10 K min^{-1}.; Figure S15: Combined calorimetric activation plot for the TMFSC and TMDSC.; Figure S16: Dielectric loss spectra at a frequency of 1000 Hz for selected samples.; Figure S17: Activation plot for the β-relaxation and γ-relaxation.; Figure S18: Combined α-relaxation plot with the α- and α*-process.; Table S1: McSAS fit average values for the D_{sheet}, D_{lumen} and D_{outer} for the nanofillers and the epoxy nanocomposites.

Institutional Review Board Statement: Not applicable.

Informed Consent Statement: Not applicable.

Data Availability Statement: The data presented in this study are available on request from the corresponding author.

Conflicts of Interest: The authors declare that there is no conflict of interest.

References

1. Mittal, V. Polymer Nanocomposites: Synthesis, Microstructure, and Properties. In *Optimization of Polymer Nanocomposite Properties*; Mittal, V., Ed.; Wiley-VCH Verlag GmbH & Co. KgaA: Weinheim, Germany, 2010; p. 1. ISBN 978-3-52762-927-5.
2. Dantas de Oliveira, A.; Augusto Gonçalves Beatrice, C. Polymer Nanocomposites with Different Types of Nanofiller. In *Nanocomposites-Recent Evolutions*; Sivasankaran, S., Ed.; IntechOpen: London, UK, 2019; p. 26. ISBN 978-1-78985-012-3.
3. Müller, K.; Bugnicourt, E.; Latorre, M.; Jorda, M.; Echegoyen Sanz, Y.; Lagaron, J.M.; Miesbauer, O.; Bianchin, A.; Hankin, S.; Bölz, U.; et al. Review on the Processing and Properties of Polymer Nanocomposites and Nanocoatings and Their Applications in the Packaging, Automotive and Solar Energy Fields. *Nanomaterials* **2017**, *7*, 74. [CrossRef]
4. Bailey, E.J.; Winey, K.I. Dynamics of polymer segments, polymer chains, and nanoparticles in polymer nanocomposite melts: A review. *Prog. Polym. Sci.* **2020**, *105*, 101242. [CrossRef]
5. Kumar, S.K.; Benicewicz, B.C.; Vaia, R.A.; Winey, K.I. 50th Anniversary Perspective: Are Polymer Nanocomposites Practical for Applications? *Macromolecules* **2017**, *50*, 714–731. [CrossRef]
6. Šupová, M.; Simha Martynková, G.; Cech Barabaszova, K. Effect of Nanofillers Dispersion in Polymer Matrices: A Review. *Sci. Adv. Mater.* **2010**, *3*, 1–25. [CrossRef]
7. Deng, S.; Zhang, J.; Ye, L. Halloysite–epoxy nanocomposites with improved particle dispersion through ball mill homogenisation and chemical treatments. *Compos. Sci. Technol.* **2009**, *69*, 2497–2505. [CrossRef]
8. Jana, S.C.; Jain, S. Dispersion of nanofillers in high performance polymers using reactive solvents as processing aids. *Polymer* **2001**, *42*, 6897–6905. [CrossRef]
9. Zare, Y. Study of nanoparticles aggregation/agglomeration in polymer particulate nanocomposites by mechanical properties. *Compos. Part A Appl. Sci. Manuf.* **2016**, *84*, 158–164. [CrossRef]
10. Dorigato, A.; Dzenis, Y.; Pegoretti, A. Filler aggregation as a reinforcement mechanism in polymer nanocomposites. *Mech. Mater.* **2013**, *61*, 79–90. [CrossRef]

11. Szymoniak, P.; Qu, X.; Abbasi, M.; Pauw, B.R.; Henning, S.; Li, Z.; Wang, D.-Y.; Schick, C.; Saalwächter, K.; Schönhals, A. Spatial inhomogeneity, interfaces and complex vitrification kinetics in a network forming nanocomposite. *Soft Matter* **2021**, *17*, 2775–2790. [CrossRef] [PubMed]

12. Koutsoumpis, S.; Raftopoulos, K.N.; Oguz, O.; Papadakis, C.M.; Menceloglu, Y.Z.; Pissis, P. Dynamic glass transition of the rigid amorphous fraction in polyurethane-urea/SiO2 nanocomposites. *Soft Matter* **2017**, *13*, 4580–4590. [CrossRef] [PubMed]

13. Purohit, P.J.; Wang, D.-Y.; Wurm, A.; Schick, C.; Schönhals, A. Comparison of thermal and dielectric spectroscopy for nanocomposites based on polypropylene and Layered Double Hydroxide–Proof of interfaces. *Eur. Polym. J.* **2014**, *55*, 48–56. [CrossRef]

14. Fragiadakis, D.; Pissis, P. Glass transition and segmental dynamics in poly(dimethylsiloxane)/silica nanocomposites studied by various techniques. *J. Non. Cryst. Solids* **2007**, *353*, 4344–4352. [CrossRef]

15. Yin, H.; Schönhals, A. Broadband Dielectric Spectroscopy on Polymer Blends. In *Polymer Blends Handbook*; Utracki, L.A., Wilkie, C.A., Eds.; Springer: Dordrecht, The Netherlands, 2014; pp. 1299–1356. ISBN 978-94-007-6064-6.

16. Koshy, O.; Subramanian, L.; Thomas, S. Differential Scanning Calorimetry in Nanoscience and Nanotechnology. In *Thermal and Rheological Measurement Techniques for Nanomaterials Characterization*; Thomas, S., Thomas, R., Zachariah, A.K., Mishra, R.K., Eds.; Micro and Nano Technologies; Elsevier: Amsterdam, The Netherlands, 2017; pp. 109–122. ISBN 978-0-323-46139-9.

17. Mathot, V.; Pyda, M.; Pijpers, T.; Vanden Poel, G.; van de Kerkhof, E.; van Herwaarden, S.; van Herwaarden, F.; Leenaers, A. The Flash DSC 1, a power compensation twin-type, chip-based fast scanning calorimeter (FSC): First findings on polymers. *Thermochim. Acta* **2011**, *522*, 36–45. [CrossRef]

18. Schick, C. Chapter 16-Temperature modulated differential scanning calorimetry (TMDSC)–basics and applications to polymers. In *Handbook of Thermal Analysis and Calorimetry. Volume 3: Applications to Polymers and Plastics*; Cheng, S.Z.D., Ed.; Handbook of Thermal Analysis and Calorimetry; Elsevier Science B.V.: Amsterdam, The Netherlands, 2002; Volume 3, pp. 713–810.

19. Thermal Analysis of Polymeric Materials, 1st ed.Springer-Verlag: Berlin/Heidelberg, Germany, 2005; ISBN 978-3-540-23629-0.

20. Piscitelli, F.; Lavorgna, M.; Buonocore, G.G.; Verdolotti, L.; Galy, J.; Mascia, L. Plasticizing and Reinforcing Features of Siloxane Domains in Amine-Cured Epoxy/Silica Hybrids. *Macromol. Mater. Eng.* **2013**, *298*, 896–909. [CrossRef]

21. Gu, H.; Ma, C.; Gu, J.; Guo, J.; Yan, X.; Huang, J.; Zhang, Q.; Guo, Z. An overview of multifunctional epoxy nanocomposites. *J. Mater. Chem. C* **2016**, *4*, 5890–5906. [CrossRef]

22. Wetzel, B.; Rosso, P.; Haupert, F.; Friedrich, K. Epoxy nanocomposites–fracture and toughening mechanisms. *Eng. Fract. Mech.* **2006**, *73*, 2375–2398. [CrossRef]

23. Saba, N.; Jawaid, M.; Alothman, O.Y.; Paridah, M.T.; Hassan, A. Recent advances in epoxy resin, natural fiber-reinforced epoxy composites and their applications. *J. Reinf. Plast. Compos.* **2016**, *35*, 447–470. [CrossRef]

24. Yao, H.-Y.; Lin, Y.-W.; Chang, T.-H. Dielectric Properties of BaTiO3–Epoxy Nanocomposites in the Microwave Regime. *Polymers* **2021**, *13*, 1391. [CrossRef]

25. Chen, C.; Justice, R.S.; Schaefer, D.W.; Baur, J.W. Highly dispersed nanosilica–epoxy resins with enhanced mechanical properties. *Polymer* **2008**, *49*, 3805–3815. [CrossRef]

26. Ghasem Zadeh Khorasani, M.; Silbernagl, D.; Szymoniak, P.; Hodoroaba, V.-D.; Sturm, H. The effect of boehmite nanoparticles (γ-AlOOH) on nanomechanical and thermomechanical properties correlated to crosslinking density of epoxy. *Polymer* **2019**, *164*, 174–182. [CrossRef]

27. Szymoniak, P.; Pauw, B.R.; Qu, X.; Schönhals, A. Competition of nanoparticle-induced mobilization and immobilization effects on segmental dynamics of an epoxy-based nanocomposite. *Soft Matter* **2020**, *16*, 5406–5421. [CrossRef] [PubMed]

28. Szymoniak, P.; Li, Z.; Wang, D.-Y.; Schönhals, A. Dielectric and flash DSC investigations on an epoxy based nanocomposite system with MgAl layered double hydroxide as nanofiller. *Thermochim. Acta* **2019**, *677*, 151–161. [CrossRef]

29. Ramirez, C.; Rico, M.; Torres, A.; Barral, L.; Lopez, J.; Montenero, B. Epoxy/POSS organic–inorganic hybrids: ATR-FTIR and DSC studies. *Eur. Polym. J.* **2008**, *44*, 3035–3045. [CrossRef]

30. Han, X.; Zhang, X.; Guo, Y.; Liu, X.; Zhao, X.; Zhou, H.; Zhang, S.; Zhao, T. Synergistic Effects of Ladder and Cage Structured Phosphorus-Containing POSS with Tetrabutyl Titanate on Flame Retardancy of Vinyl Epoxy Resins. *Polymers* **2021**, *13*, 1363. [CrossRef] [PubMed]

31. Shen, J.; Huang, W.; Wu, L.; Hu, Y.; Ye, M. Thermo-physical properties of epoxy nanocomposites reinforced with amino-functionalized multi-walled carbon nanotubes. *Compos. Part A Appl. Sci. Manuf.* **2007**, *38*, 1331–1336. [CrossRef]

32. Irzhak, V.I.; Dzhardimalieva, G.I.; Uflyand, I.E. Structure and properties of epoxy polymer nanocomposites reinforced with carbon nanotubes. *J. Polym. Res.* **2019**, *26*, 220. [CrossRef]

33. Cividanes, L.S.; Simonetti, E.A.N.; Moraes, M.B.; Fernandes, F.W.; Thim, G.P. Influence of carbon nanotubes on epoxy resin cure reaction using different techniques: A comprehensive review. *Polym. Eng. Sci.* **2014**, *54*, 2461–2469. [CrossRef]

34. Yuan, P.; Tan, D.; Annabi-Bergaya, F. Properties and applications of halloysite nanotubes: Recent research advances and future prospects. *Appl. Clay Sci.* **2015**, *112–113*, 75–93. [CrossRef]

35. Du, M.; Guo, B.; Jia, D. Thermal stability and flame retardant effects of halloysite nanotubes on poly(propylene). *Eur. Polym. J.* **2006**, *42*, 1362–1369. [CrossRef]

36. Li, Z.; Liu, L.; Jiménez González, A.; Wang, D.-Y. Bioinspired polydopamine-induced assembly of ultrafine Fe(OH)3 nanoparticles on halloysite toward highly efficient fire retardancy of epoxy resin via an action of interfacial catalysis. *Polym. Chem.* **2017**, *8*, 3926–3936. [CrossRef]

37. Ye, Y.; Chen, H.; Wu, J.; Ye, L. High impact strength epoxy nanocomposites with natural nanotubes. *Polymer* **2007**, *48*, 6426–6433. [CrossRef]
38. Lvov, Y.; Abdullayev, E. Functional polymer–clay nanotube composites with sustained release of chemical agents. *Prog. Polym. Sci.* **2013**, *38*, 1690–1719. [CrossRef]
39. Vijayan, P.P.; Hany El-Gawady, Y.M.; Al-Maadeed, M.A.S.A. Halloysite Nanotube as Multifunctional Component in Epoxy Protective Coating. *Ind. Eng. Chem. Res.* **2016**, *55*, 11186–11192. [CrossRef]
40. Deng, S.; Zhang, J.; Ye, L.; Wu, J. Toughening epoxies with halloysite nanotubes. *Polymer* **2008**, *49*, 5119–5127. [CrossRef]
41. Liu, M.; Guo, B.; Du, M.; Cai, X.; Jia, D. Properties of halloysite nanotube–epoxy resin hybrids and the interfacial reactions in the systems. *Nanotechnology* **2007**, *18*, 455703. [CrossRef]
42. Ravichandran, G.; Rathnakar, G.; Santhosh, N.; Chennakeshava, R.; Hashmi, M.A. Enhancement of mechanical properties of epoxy/halloysite nanotube (HNT) nanocomposites. *SN Appl. Sci.* **2019**, *1*. [CrossRef]
43. Akbari, V.; Jouyandeh, M.; Paran, S.M.R.; Ganjali, M.R.; Abdollahi, H.; Vahabi, H.; Ahmadi, Z.; Formela, K.; Esmaeili, A.; Mohaddespour, A.; et al. Effect of Surface Treatment of Halloysite Nanotubes (HNTs) on the Kinetics of Epoxy Resin Cure with Amines. *Polymers* **2020**, *12*, 930. [CrossRef]
44. Liu, M.; Jia, Z.; Jia, D.; Zhou, C. Recent advance in research on halloysite nanotubes-polymer nanocomposite. *Prog. Polym. Sci.* **2014**, *39*, 1498–1525. [CrossRef]
45. Lee, H.; Dellatore, S.M.; Miller, W.M.; Messersmith, P.B. Mussel-Inspired Surface Chemistry for Multifunctional Coatings. *Science* **2007**, *318*, 426–430. [CrossRef]
46. Barclay, T.G.; Hegab, H.M.; Clarke, S.R.; Ginic-Markovic, M. Versatile Surface Modification Using Polydopamine and Related Polycatecholamines: Chemistry, Structure, and Applications. *Adv. Mater. Interfaces* **2017**, *4*, 1601192. [CrossRef]
47. Du, M.; Guo, B.; Jia, D. Newly emerging applications of halloysite nanotubes: A review. *Polym. Int.* **2010**, *59*, 574–582. [CrossRef]
48. Phantom Plastics Halloysite Clay Nanotubes. Available online: https://phantomplastics.com/functional-fillers/halloysite/ (accessed on 30 March 2021).
49. Filik, J.; Ashton, A.W.; Chang, P.C.Y.; Chater, P.A.; Day, S.J.; Drakopoulos, M.; Gerring, M.W.; Hart, M.L.; Magdysyuk, O.V.; Michalik, S.; et al. Processing two-dimensional X-ray diffraction and small-angle scattering data in *DAWN 2*. *J. Appl. Crystallogr.* **2017**, *50*, 959–966. [CrossRef]
50. Bressler, I.; Pauw, B.R.; Thünemann, A.F. *McSAS*: Software for the retrieval of model parameter distributions from scattering patterns. *J. Appl. Crystallogr.* **2015**, *48*, 962–969. [CrossRef]
51. Aratsu, K.; Takeya, R.; Pauw, B.R.; Hollamby, M.J.; Kitamoto, Y.; Shimizu, N.; Takagi, H.; Haruki, R.; Adachi, S.; Yagai, S. Supramolecular copolymerization driven by integrative self-sorting of hydrogen-bonded rosettes. *Nat. Commun.* **2020**, *11*, 1623. [CrossRef] [PubMed]
52. Ma, W.; Wu, H.; Higaki, Y.; Takahara, A. Halloysite Nanotubes: Green Nanomaterial for Functional Organic-Inorganic Nanohybrids. *Chem. Rec.* **2018**, *18*, 986–999. [CrossRef] [PubMed]
53. Zhang, H. Selective modification of inner surface of halloysite nanotubes: A review. *Nanotechnol. Rev.* **2017**, *6*, 573–581. [CrossRef]
54. Debye, P. Zerstreuung von Röntgenstrahlen. *Ann. Phys.* **1915**, *351*, 809–823. [CrossRef]
55. Hansen, S. Calculation of small-angle scattering profiles using Monte Carlo simulation. *J. Appl. Crystallogr.* **1990**, *23*, 344–346. [CrossRef]
56. OpenSCAD. Available online: Openscad.org (accessed on 31 March 2021).
57. Schönhals, A. Dielectric Spectroscopy on the Dynamics of Amorphous Polymeric Systems. *Appl. Note Dielectr.* **1998**, *1*, 1–17.
58. Sun, P.; Liu, G.; Lv, D.; Dong, X.; Wu, J.; Wang, D. Effective activation of halloysite nanotubes by piranha solution for amine modification via silane coupling chemistry. *RSC Adv.* **2015**, *5*, 52916–52925. [CrossRef]
59. Abdullayev, E.; Joshi, A.; Wei, W.; Zhao, Y.; Lvov, Y. Enlargement of Halloysite Clay Nanotube Lumen by Selective Etching of Aluminum Oxide. *ACS Nano* **2012**, *6*, 7216–7226. [CrossRef]
60. Stewart, G.W. Theory of X-Ray Diffraction in Liquids. *Phys. Rev.* **1928**, *32*, 558–563. [CrossRef]
61. Sun, Y.; Zhang, Z.; Moon, K.-S.; Wong, C.P. Glass transition and relaxation behavior of epoxy nanocomposites. *J. Polym. Sci. Part B Polym. Phys.* **2004**, *42*, 3849–3858. [CrossRef]
62. Maggana, C.; Pissis, P. TSDC studies of the effects of plasticizer and water on the sub-Tg relaxations of an epoxy resin system. *J. Macromol. Sci. Part B* **1997**, *36*, 749–772. [CrossRef]
63. Wunderlich, B. Reversible crystallization and the rigid–amorphous phase in semicrystalline macromolecules. *Prog. Polym. Sci.* **2003**, *28*, 383–450. [CrossRef]
64. Alhabill, F.N.; Ayoob, R.; Andritsch, T.; Vaughan, A.S. Influence of filler/matrix interactions on resin/hardener stoichiometry, molecular dynamics, and particle dispersion of silicon nitride/epoxy nanocomposites. *J. Mater. Sci.* **2018**, *53*, 4144–4158. [CrossRef]
65. Hanzon, D.W.; Yu, K.; Yakacki, C.M. Chapter Five-Activation Mechanisms of Shape-Memory Polymers. In *Shape-Memory Polymer Device Design*; Safranski, D.L., Griffis, J.C., Eds.; Plastics Design Library, William Andrew Publishing: Norwich, NY, USA, 2017; pp. 139–187. ISBN 978-0-323-37797-3.
66. Vogel, H. Das Temperaturabhangigkeitsgesetz der Viskositat von Flussigkeiten. *Phys. Z.* **1921**, *22*, 645–646.
67. Fulcher, G.S. Analysis of Recent Measurements of the Viscosity of Glasses. *J. Am. Ceram. Soc.* **1925**, *8*, 339–355. [CrossRef]

68. Tammann, G.; Hesse, W. Die Abhängigkeit der Viscosität von der Temperatur bei unterkühlten Flüssigkeiten. *Z. Anorg. Allg. Chem.* **1926**, *156*, 245–257. [CrossRef]

69. Havriliak, S.; Negami, S. A complex plane analysis of α-dispersions in some polymer systems. *J. Polym. Sci. Part C Polym. Symp.* **1966**, *14*, 99–117. [CrossRef]

70. Havriliak, S.; Negami, S. A complex plane representation of dielectric and mechanical relaxation processes in some polymers. *Polymer* **1967**, *8*, 161–210. [CrossRef]

71. Ochi, M.; Okazaki, M.; Shimbo, M. Mechanical relaxation mechanism of epoxide resins cured with aliphatic diamines. *J. Polym. Sci. Polym. Phys. Ed.* **1982**, *20*, 689–699. [CrossRef]

72. Ochi, M.; Yoshizumi, M.; Shimbo, M. Mechanical and dielectric relaxations of epoxide resins containing the spiro-ring structure. II. Effect of the introduction of methoxy branches on low-temperature relaxations of epoxide resins. *J. Polym. Sci. Part B Polym. Phys.* **1987**, *25*, 1817–1827. [CrossRef]

73. Mangion, M.B.M.; Johari, G.P. Relaxations of thermosets. III. Sub-Tg dielectric relaxations of bisphenol-A–based epoxy cured with different cross-linking agents. *J. Polym. Sci. Part B Polym. Phys.* **1990**, *28*, 71–83. [CrossRef]

74. Heijboer, J. Molecular Basis of Transitions and Relaxation. In *Midland Macromolecular Monographs*; Meier, D.J., Ed.; Gordon and Breach Science Publishers: New York, NY, USA, 1978; ISBN 9780677112404.

75. Hassan, M.K.; Tucker, S.J.; Abukmail, A.; Wiggins, J.S.; Mauritz, K.A. Polymer chain dynamics in epoxy based composites as investigated by broadband dielectric spectroscopy. *Arab. J. Chem.* **2016**, *9*, 305–315. [CrossRef]

76. Patil, P.N.; Rath, S.K.; Sharma, S.K.; Sudarshan, K.; Maheshwari, P.; Patri, M.; Praveen, S.; Khandelwal, P.; Pujari, P.K. Free volumes and structural relaxations in diglycidyl ether of bisphenol-A based epoxy–polyether amine networks. *Soft Matter* **2013**, *9*, 3589–3599. [CrossRef]

77. Wübbenhorst, M.; van Turnhout, J. "Conduction-free" dielectric loss de/dlnf-a powerful tool for the analysis of strong (ion) conducting dielectric materials. *Dielectr. Newsl.* **2000**, *14*, 1–8.

78. Klonos, P.; Panagopoulou, A.; Bokobza, L.; Kyritsis, A.; Peoglos, V.; Pissis, P. Comparative studies on effects of silica and titania nanoparticles on crystallization and complex segmental dynamics in poly(dimethylsiloxane). *Polymer* **2010**, *51*, 5490–5499. [CrossRef]

79. Fragiadakis, D.; Bokobza, L.; Pissis, P. Dynamics near the filler surface in natural rubber-silica nanocomposites. *Polymer* **2011**, *52*, 3175–3182. [CrossRef]

80. Donth, E. The size of cooperatively rearranging regions at the glass transition. *J. Non. Cryst. Solids* **1982**, *53*, 325–330. [CrossRef]

81. Schawe, J.E.K. Vitrification in a wide cooling rate range: The relations between cooling rate, relaxation time, transition width, and fragility. *J. Chem. Phys.* **2014**, *141*, 184905. [CrossRef] [PubMed]

82. Akbari, V.; Najafi, F.; Vahabi, H.; Jouyandeh, M.; Badawi, M.; Morisset, S.; Ganjali, M.R.; Saeb, M.R. Surface chemistry of halloysite nanotubes controls the curability of low filled epoxy nanocomposites. *Prog. Org. Coat.* **2019**, *135*, 555–564. [CrossRef]

83. Yang, L.; Phua, S.L.; Teo, J.K.H.; Toh, C.L.; Lau, S.K.; Ma, J.; Lu, X. A Biomimetic Approach to Enhancing Interfacial Interactions: Polydopamine-Coated Clay as Reinforcement for Epoxy Resin. *ACS Appl. Mater. Interfaces* **2011**, *3*, 3026–3032. [CrossRef] [PubMed]